

# Computational Model of DIC Microscopy: From Observations to Measurements

Farhana Kagalwala

Frederick Lanni

Takeo Kanade

Robotics Institute  
Carnegie Mellon University  
farhana@cs.cmu.edu

Center for Light Microscope  
Imaging and Biotechnology  
and Dept. of Biological Sciences  
Carnegie Mellon University

Robotics Institute  
Carnegie Mellon University

CMU-RI Tech Report TR-00-10

## Abstract

Although Differential Interference Contrast (DIC) microscopy is a powerful visualization tool used to study live biological cells, its use so far has been limited to qualitative observations. The inherent non-linear relation between the object properties and the image intensity makes quantitative analysis difficult. Towards quantitatively measuring optical properties of objects from DIC images, we develop a model for the DIC image formation process using methods consistent with energy conservation laws. We verify our model by comparing real image data of manufactured specimens with simulated images of virtual objects. We plan to use this model to iteratively reconstruct the three-dimensional properties of unknown specimens.

Key words:

## 1. Introduction

The Nomarski differential interference contrast (DIC) microscope is the preferred method for visualizing live biological specimens. The DIC microscope is an interferometer, therefore the refractive structure of the specimen is made visible. In biological research, live, transparent cells can be imaged with this microscope modality. Three-dimensional structure can be visualized by optically-sectioning<sup>†</sup> through the specimen. To date, however, biologists only qualitatively assess DIC images of cell specimens. The inherent non-linearities in the DIC image formation process have hindered past attempts at quantitative analysis. In this paper, we describe a computational model of the DIC imaging process. The model is the first step in quantitatively reconstructing properties of the specimen viewed under the DIC microscope.

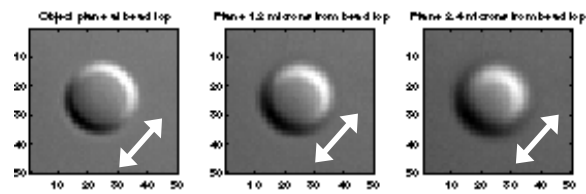


Fig. 1. Example DIC Image of Bead: The specimen contained a  $10\mu\text{m}$  polystyrene bead embedded in optical cement, with refractive index difference of .03. The leftmost image has the bead in focus while in the other two images the bead is increasingly de-focused. The arrow indicates the shear direction.

DIC microscopy offers several advantages over other contrast-generating optical systems. Due to higher axial resolution, thick specimens with three-dimensional features are better resolved with DIC than with brightfield microscopy. In DIC the pupil is unobstructed, therefore transverse<sup>†</sup> and axial resolution exceeds that in Zernike phase contrast. In contrast to fluorescence methods, no dyes are injected and therefore live specimens are not adversely

---

<sup>†</sup>For each image in an optically-sectioned set, the optical elements are configured to focus at a particular object distance.

<sup>†</sup>Transverse planes are perpendicular to the optical axis of the microscope

affected. Finally, unlike the slow rates of acquisition in confocal scanning methods, an entire stack of optically-sectioned images can be acquired within a minute. In the case of mobile cells, the short acquisition time minimizes distortions between optically-sectioned slices.

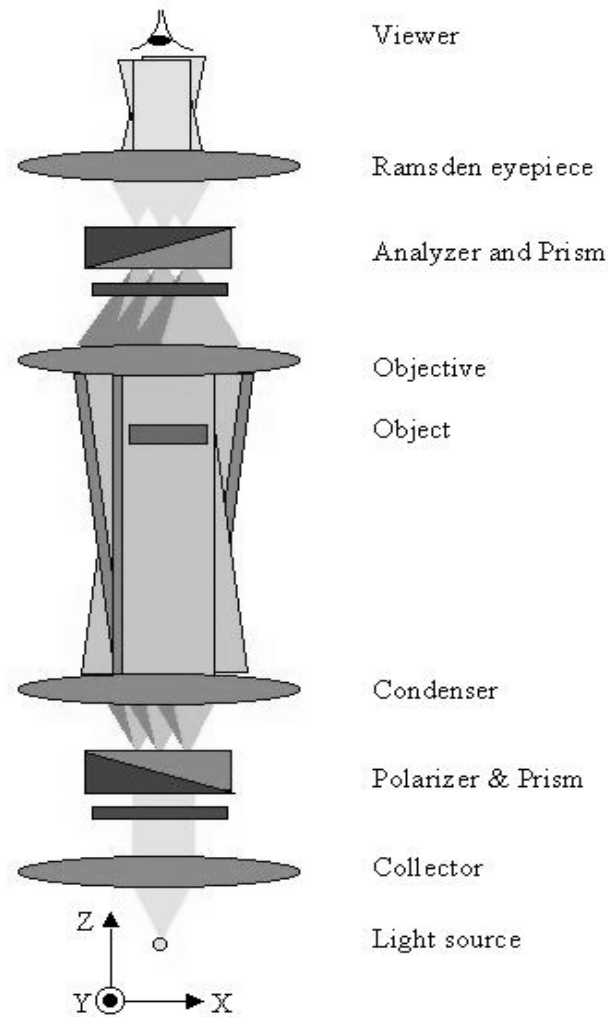


Fig. 2. DIC Optical Components: Regular brightfield microscope components such as a light source, collector, condenser, objective and eyepiece are supplemented with a pair of polarizer-prism set. Each lens element shown may actually be composed of multiple optical elements. Three colored light paths are shown to illustrate conjugate planes of reference. Optical elements and spacing are not to scale.

Looking through the eyepiece of the DIC microscope, an observer sees the differential of the optical path length introduced by the object into the propagating light wave. The differential is along a particular direction, in the transverse plane, called the shear direction. The DIC microscope [Figure 2], is essentially a brightfield microscope with a polarizer-analyzer pair and two prisms. As in standard brightfield optics, light from a lamp is collimated by a collector and a condenser lens combination. In DIC, a polarizer and a Wollaston prism is inserted between the collector and condenser lens. Moreover, the prism is positioned with respect to the back focal plane of the condenser. The described setup produces two diverging wavefronts, each field polarized perpendicularly with respect to the other field, from each point in the condenser's back focal plane. After transformation by the condenser, the wavefronts are differentially translated with respect to each other. The amount of translation is the shear amount and the direction of translation is the shear direction. Both wavefronts propagate through the specimen. In front of the objective lens, an analyzer and Nomarski prism are inserted and aligned with the front focal plane of the objective. This combination produces a steady pattern of interference between the two wavefronts which can then be detected by a CCD camera or the human eye. The Nomarski prism is a Wollaston prism modified to compensate for the fact that the objective lens' front focal plane is embedded within the lens' case and is inaccessible. Conceptually, the Nomarski prism and the first Wollaston prism are identical. The Wollaston prism behind the condenser introduces a linear phase gradient across the two fields emerging from the condenser. The Nomarski prism, in front of the objective lens compensates for this linear phase gradient. Therefore, the combined action of the two prisms results in a constant phase bias between the two perpendicularly polarized fields.

Mathematically, the DIC imaging process can be summarized by the following set of equations. First, consider a coherent field represented by

$$U_{ill}(\vec{x}) = A \exp[-i\phi_{ill}(\vec{x})]. \quad (1)$$

where  $\vec{x} = (x, y, z)$  are spatial variables in the coordinate space of the object with the  $z$ -axis

coincident with the optical axis.  $\phi(\vec{x})$  is the phase function. The action of the two prisms can be represented as an aggregate by  $U_{ill}^1(\vec{x})$  and  $U_{ill}^2(\vec{x})$ , where

$$U_{ill}^1(\vec{x}) = A \exp[-i[\phi_{ill}(\vec{x} + \vec{v}_s) + \Delta\phi_{bias}]] \quad (2)$$

$$U_{ill}^2(\vec{x}) = A \exp[-i\phi_{ill}(\vec{x} - \vec{v}_s)] \quad (3)$$

In the above equations,  $\Delta\phi_{bias}$  is the constant phase bias and  $2\vec{v}_s$  is the shear vector. The shear vector is a vector along the shear direction with a magnitude equal to the shear amount. After a phase transformation,  $\phi_{obj}(\vec{x})$ , due to the object, the wavefronts

$$U_{obj}^1(\vec{x}) = A \exp[-i[\phi_{obj}(\vec{x} + \vec{v}_s) + \Delta\phi_{bias}]] \quad (4)$$

$$U_{obj}^2(\vec{x}) = A \exp[-i\phi_{obj}(\vec{x} - \vec{v}_s)]. \quad (5)$$

contain the object information. The field in the image space is

$$U_{img}(\vec{x}_{img}) = \int_{y_0^{obj}}^{y_1^{obj}} \int_{x_0^{obj}}^{x_1^{obj}} K_z(x_{img}, y_{img}; x, y) [U_{obj}^1(x, y, z = z_1) - U_{obj}^2(x, y, z = z_1)] dx dy \quad (6)$$

where  $K_z(x_{img}, y_{img}, x, y)$  is the complex amplitude point spread function of the imaging system (objective and any other auxiliary lens) of the microscope.  $\vec{x}_{img} = (x_{img}, y_{img}, z_{img})$  are spatial variables in the coordinate space of the image with the  $z_{img}$ -axis coincident with the optical axis.  $K_z(\dots)$  describes the propagation from the object plane at  $z = z_1$  to the image plane  $z_{img}$ . The image intensity  $I(\vec{x}_{img})$  is

$$I(\vec{x}_{img}) = |U_{img}(x_{img}, y_{img}, z_{img})|^2 \quad (7)$$

The nonlinearity in the DIC image has two basic sources. First, since the image is an interference pattern, the detected intensity is the squared magnitude of the light field's complex amplitude. Therefore, a convolution of the light intensity with a lens transfer function does not accurately represent the DIC image, which is a linear superposition of complex amplitude, rather than intensity, components of the light field. In addition, out of focus contributions from the object have to be considered. Therefore a three-dimensional amplitude point spread (or transmission) function is needed to accurately model the image intensity.

Second, the object itself aberrates the light wave as it propagates through. The biological specimens under consideration, though weakly refractive, are thick and scatter light significantly. Therefore, aberrations due to the object contribute significantly to the image. An accurate model has to take the scattering properties of the object into consideration.

We attempt to address each of the above complications. Using a generalized ray tracing method we have developed a model of light propagation through the specimen. Based on energy-conservation laws, the light paths are traced through the object. Diffracted wavefronts at the objective plane are numerically approximated and the resulting intensity distribution at the image plane is calculated. We evaluate this model by comparing real data and simulated images of actual and virtual three dimensional objects, respectively. This model is currently being used to reconstruct the three-dimensional refractive-index distribution of the specimen.

## 2. Previous Work

Deconvolution methods, such as computational optical sectioning microscopy (COSM), are widely used to recover object information from images acquired by certain optical modalities. COSM methods model the image intensity as a convolution of the object's intensity transmittance with a computed point-spread function. In modalities such as fluorescence and brightfield, a linear function of the intensity from the object provides an accurate, first order approximation of the image. However, in DIC microscopy, the image cannot be represented by merely considering the intensity from the object, as explained above. Both phase and amplitude information have to be modelled.

One of the earliest models of DIC optics was formulated by Galbraith in 1982<sup>11</sup>. Under assumptions of a thin object<sup>†</sup> a complex amplitude point spread function is formulated in the work. A signal-processing model for DIC optics was formulated by Holmes and Levy in

---

<sup>†</sup>The axial thickness of a thin object is less than the objective's depth of field

1987<sup>14</sup>. They assumed a coherent illumination model, in addition to the earlier assumptions by Galbraith, and formulated a transfer function to represent DIC optics in the Fourier domain. In recent years, Cogswell and Sheppard extended previous models of DIC optics to include partially-coherent illumination<sup>6</sup>.

In 1996, Feinegle used a contour finding algorithm to locate edges in each image from an optically-sectioned stack<sup>9</sup>. In this work, specimen structure is obtained by axial integration of contours. Also, in this work, each image in the stack was filtered to reveal in-focus features, and therefore some attempt was made to model the object in three-dimensions. The most recent work in the analysis of DIC images is by Preza<sup>21</sup>. This work recovers the optical path-length at each image point due to the object.

The only attempt to quantify information from DIC optics has been made by Cogswell, et. al. using optical techniques referred to as geometric phase methods.<sup>5</sup> Though we are unaware of cases where this method has been applied to recover three dimensional object information. The work by Feinegle produced a three dimensional model of the specimen, but the object properties were not quantitated and the recovered specimen model was not validated with ground truth experiments. Preza's work recovers optical path-length but does not actually reconstruct three dimensional object information. So far, no attempt has been made to quantitatively reconstruct the three dimensional properties of the object from DIC images. In contrast, we have developed a computational model of the DIC imaging process with the explicit intention of using it to recover three dimensional object information.

### **3. Computational Model**

Our computational model consists of a polarized ray tracer and an approximation of the diffracted fields introduced in the imaging process. According to laws consistent with geometrical optics and energy conservation principles, we propagate light paths through the object approximating the field at all points of the object.

In addition, since the objects under consideration do significantly scatter light, we ap-

proximate the effect of this scatter in the imaging process by estimating the diffracted fields from all voxel points. By doing so, we incorporate wavelength dependent information in addition to the geometrical optics approximations allowing us to more accurately model DIC images.

## A. Theory

### 1. Light Propagation in Inhomogeneous Object

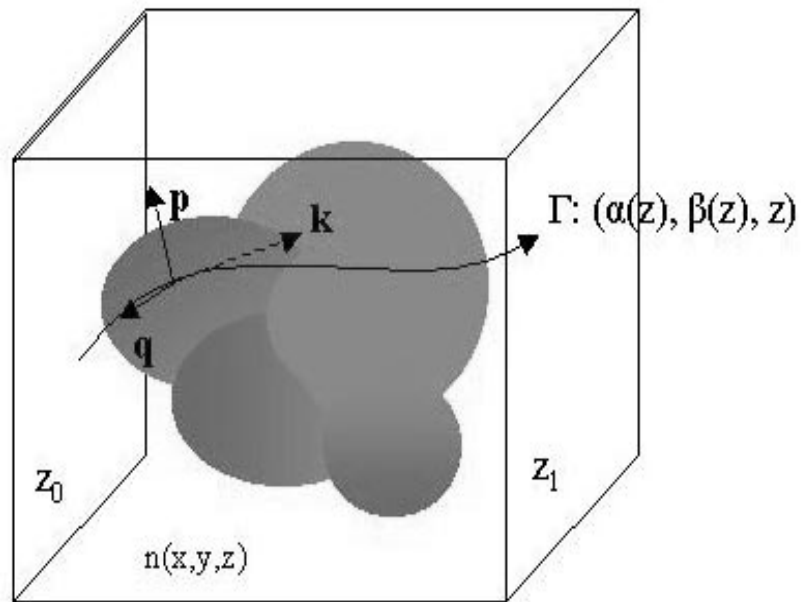


Fig. 3. Schematic of a hypothetical ray path: The entrance and exit planes are labelled  $z_0$  and  $z_1$  respectively. The local coordinate system of the ray is represented by the vectors  $\vec{k}$ ,  $\vec{p}$ , and  $\vec{q}$ . The ray path is shown as the 3-D curve  $\Gamma: (\alpha(z), \beta(z), z)$ .

Using principles of geometrical optics, we approximate light propagation through an inhomogeneous, isotropic object. A light ray, which is a three dimensional curve, represents the energy of a light field propagated along a narrow tube surrounding the ray path. Most commonly, rays are used to propagate the field's intensity along particular paths. We generalize this by computing the local polarized field along the ray path. A time-harmonic, monochromatic, polarized electric field can be represented by a vector-valued amplitude and phase. The field wavefronts are surfaces along which the phase is constant. In isotropic media, light rays are the trajectories normal to the wavefronts. The light rays are mathematically defined as the solution of a particular variational formulation. Let the refractive index distribution of the object be  $n(x, y, z)$  extending between  $z = z_0$  and  $z = z_1$ . [Fig. 3] We assume that  $n(x, y, z)$  has small variations which is consistent with live biological cells. The light rays are represented by  $, = (\alpha(z), \beta(z), z)$ . Following Fermat's principle,  $\alpha(z)$  and  $\beta(z)$  satisfy the following minimization condition of the variational integral equation:

$$\delta \int_{z_0}^{z_1} n(\alpha(z), \beta(z), z) \sqrt{\alpha'(z)^2 + \beta'(z)^2 + 1} dz = 0. \quad (8)$$

Consistent with the above condition,  $\alpha(z)$  and  $\beta(z)$  solve a set of initial-valued Euler-Lagrange differential equations. For each initial valued point,  $x_0 = \alpha(z_0)$  and  $y_0 = \beta(z_0)$  the variational problem is solved by a particular curve,  $,_p = (\alpha_p(z), \beta_p(z), z)$ . The intersection of the curve with the  $z = z_1$  plane is a point  $P_p = (x_1 = \alpha(z_1), y_1 = \beta(z_1), z)$ . In our model, rays which enter the object at a specific point with a specific angle provide the initial conditions:  $\alpha(z_0), \beta(z_0), \alpha'(z_0), \beta'(z_0)$ . These initial ray positions and angles are determined by the illuminating conditions.

In addition to  $\alpha(z), \beta(z)$  and  $n(x, y, z)$ , we define the following variables

$$\begin{aligned} n_x &= \frac{dn(x, y, z)}{dx} \\ n_y &= \frac{dn(x, y, z)}{dy} \\ n_z &= \frac{dn(x, y, z)}{dz} \\ w &= \sqrt{\left(\frac{d\alpha(z)}{dz}\right)^2 + \left(\frac{d\beta(z)}{dz}\right)^2 + 1}. \end{aligned} \quad (9)$$

The resulting differential equations are

$$\begin{aligned}\frac{d\alpha}{dz} &= \alpha_z \\ \frac{d\beta}{dz} &= \beta_z \\ \frac{d\alpha_z}{dz} &= \frac{w^3}{n(w^2 - \alpha_z)} \times \left[ n_x \left( w - \frac{\alpha_z^2}{w} \right) - n_z w \right] \\ \frac{d\beta_z}{dz} &= \frac{w^3}{n(w^2 - \beta_z)} \times \left[ n_y \left( w - \frac{\beta_z^2}{w} \right) - n_z w \right].\end{aligned}\tag{10}$$

A standard numerical integration method can be implemented to solve the above set of equations. We used the fourth-order Runge-Kutta method<sup>25</sup>. The variational method is consistent with the Hamiltonian formulation of energy conservation<sup>2</sup>. In the Hamiltonian formulation, the refractive index distribution can be regarded as the potential field. If absorption is negligible, then this is a conservative field. The gradient of the refractive index, acts as an external force on the light paths. Thus the variational formulation seeks to minimize the sum of all the forces present along the light path.

## 2. Imaging Process

In microscope systems, with image magnification typically exceeding 100X, the effects of diffraction by the objective lens cannot be ignored. The diffracted image of a point source of light in the object plane, via brightfield optics has been shown to be an Airy-disc pattern. The radius of the central peak in the pattern, as established by Lord Rayleigh, is  $\frac{1.22\lambda}{(NA_c + NA_o)}$  where  $NA_c$  is the numerical aperture of the condenser lens and  $NA_o$  is the numerical aperture of the objective lens. Using some typical values, such as light with  $\lambda = .5\mu\text{m}$ ,  $NA_c = NA_o = 1.2$  and image magnification of 200X, the radius of the pattern is approximately  $66\mu\text{m}$ . In comparison, typical scientific CCD cameras have pixel sizes between 24-7 $\mu\text{m}$ . Energy from a single point source in the object contributes significantly to multiple pixels in the image. Therefore, an accurate model of the image-formation process in a microscope system has to calculate diffraction, and consequently, wavefront dependent effects.

The image formation process in any lens system can be studied by considering light

propagation in three stages. First, the propagation of the field from the object space to the lens entrance plane. Second, the transformation introduced by the lens onto the wavefront. Third, the propagation of the field from the lens exit plane to the image space. According to Eq.6, the relation between  $U_{img}$  and  $U_{obj}$  is characterized by a kernel function,  $K_z(x_{img}, y_{img}, x, y)$ . In this section, we develop a representation for  $K_z$  by considering the propagation of the field from a point scatterer in the object space. The following discussion is based on J. Goodman's discussion of lens imaging systems<sup>12</sup>. For ease of explanation, we develop the necessary theory in reverse order.

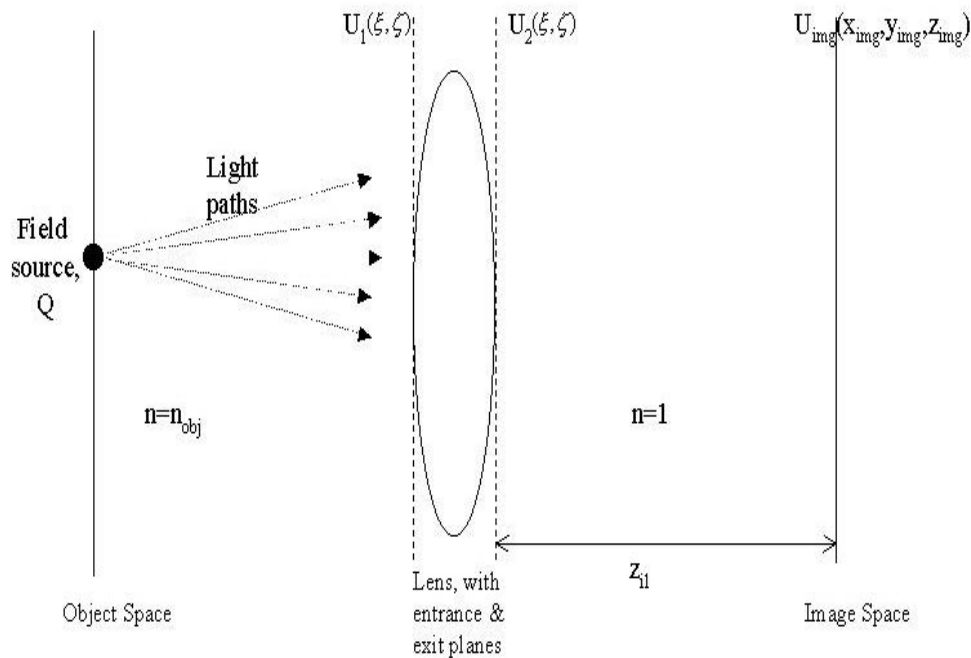


Fig. 4. Illustration of reference planes used to explain the transfer of energy from an object point to an image plane.

Given the complex amplitude of the field at the exit plane of the lens,  $U_2(\xi, \zeta)$ , assuming that the medium between the lens plane and the image plane has  $n = 1$ , the propagation

over that distance is

$$U_{img}^{z_{i1}}(x_{img}, y_{img}) = \frac{1}{i\lambda} \int \int_{-\infty}^{\infty} U_2(\xi, \zeta) \frac{\exp(ikr_i)}{r_i} \cos \theta_i d\xi d\zeta \quad (11)$$

where  $U_{img}^{z_{i1}}(x_{img}, y_{img})$  is the amplitude at a plane  $z_{img} = z_{i1}$  in the image space  $z_{i1}$  away from the lens exit plane. [Fig. 4]  $\xi$  and  $\zeta$  are the coordinates across the lens plane,  $r_i$  is the distance from each point in the lens plane to the image point  $(x_{img}, y_{img}, z_{img})$ , and  $\theta_i$  is the angle subtended by the normal to the lens plane and the vector from  $(\xi, \zeta)$  to the image point. The wave number is  $k = \frac{2\pi}{\lambda}$ . Under paraxial optics assumptions, the Fresnel approximation of the above integral is valid. Consequently, it is simplified as

$$U_{img}^{z_{i1}}(x_{img}, y_{img}) = \frac{1}{i\lambda z_i} \int \int_{-\infty}^{\infty} U_2(\xi, \zeta) \exp\left[\frac{ik}{2z_i}((x_{img} - \xi)^2 + (y_{img} - \zeta)^2)\right] d\xi d\zeta \quad (12)$$

The field at the exit plane of a thin, ideal, convex lens can be represented as a phase transformation of the field at the entrance plane of the lens. Therefore,

$$U_2(\xi, \zeta) = U_1(\xi, \zeta) \exp\left(-i\frac{k}{2f}(\xi^2 + \zeta^2)\right) \quad (13)$$

where  $U_1$  is the field at the entrance plane of the lens and  $f$  is the focal length of the lens. The above equation assumes paraxial optics. Lastly, we formulate the field at the entrance plane of the lens given the field at a point in the object space. If the medium between the object plane and the lens plane is homogeneous, then a point scatterer at the object point  $Q = (x_{obj}, y_{obj}, z_{obj})$  will give rise to a spherical wave in the entrance plane of the lens with the field distribution,

$$U_1(\xi, \zeta) = \frac{1}{i\lambda} \frac{\exp(ikn_{obj}r_o)}{r_o} \cos(\theta_{obj}). \quad (14)$$

$r_o$  is the distance from  $Q = (x_{obj}, y_{obj}, z_{obj})$  to a point  $P_0 = (\xi, \zeta)$  in the lens plane and  $n_{obj}$  is the constant refractive index of the object space.  $\theta_{obj}$  is the angle between the vector from  $Q$  to  $P_0$  and the normal to the lens plane. In homogeneous media, under paraxial optics assumptions, the above equation can be approximated by Fresnel's equations. Combining the equations from above, and ignoring the cosine term, the kernel function is

$$\begin{aligned}
K_{z_{i1}}(x_{img}, y_{img}; x, y, z) = & \frac{1}{i\lambda} \int \int_{-\infty}^{\infty} \frac{1}{r_o z_i} \exp(ik[n_{obj}r_o - \frac{1}{2f}(\xi^2 + \zeta^2) \\
& + \frac{1}{2z_i}((x_{img} - \xi)^2 + (y_{img} - \zeta)^2)]) d\xi d\zeta
\end{aligned} \tag{15}$$

If the medium between object points to the lens plane is homogeneous, the above equation for  $K_{z_{i1}}(x_{img}, y_{img}; x, y, z)$  can be approximated by the Frauhoffer diffraction integral. However, for an arbitrary refractive index distribution in the object space there is no analytical formulation for the imaging equation, and approximate numerical solutions must be pursued.

## 3. Approximations

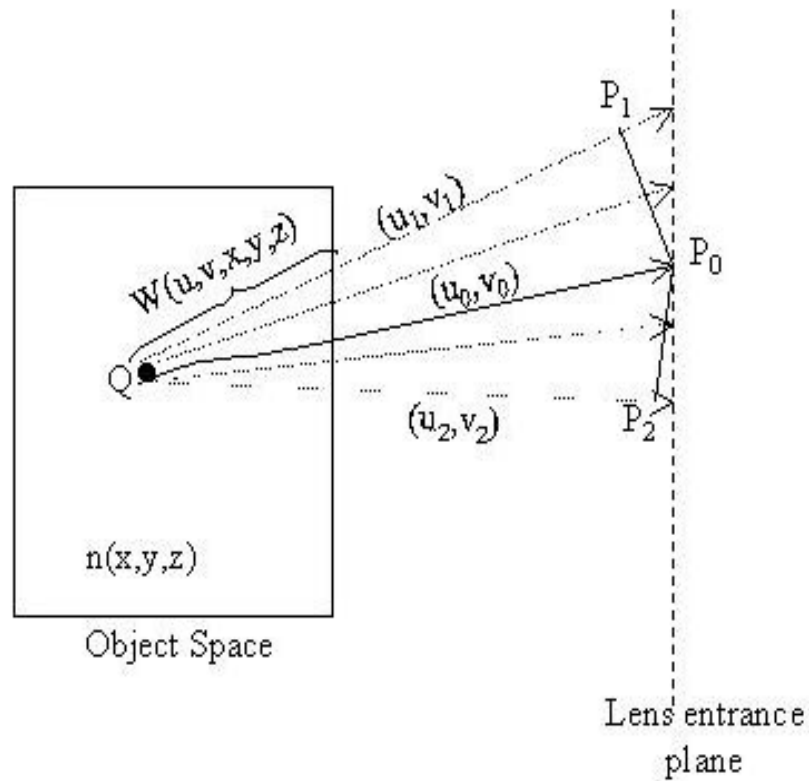


Fig. 5. Illustration of contributions to a point in the lens plane  $P_0$  from fields travelling in different directions from object point  $Q$ . The optical pathlength at  $P_0$  from each field in the direction  $(u_i, v_i)$  is the optical pathlength from  $Q$  to  $P_i$ .

Though biological cells are weakly refractive, the refractive index variations do cause distortions in the image. Any attempt to accurately simulate images must consider distortions.

tions by the object. Therefore, we incorporate a first-order contribution to the field due to diffraction by the object. In inhomogeneous media, the field at the entrance plane of the lens can be approximated using the Kline-Luneberg asymptotic evaluation of the diffraction integral. Here the diffraction is due to the object inhomogeneities. In full form, the field at any point in the lens plane can be represented by amplitude and phase contributions from rays originating at an object point and travelling in different directions. [Fig. 5] In this development,  $u$  and  $v$  are used to denote the components of the ray direction projected onto the  $x$  and  $y$  axis. For a ray emerging from the object source point  $Q$ , the field at a point on the lens plane  $P_0$ , with coordinates  $(\xi, \zeta)$ , is

$$U_1(\xi, \zeta) = \frac{ik}{2\pi} \iint_D A(u, v, w) \exp ik\Phi(u, v, \xi, \zeta, z) dudv \quad (16)$$

where  $A(u, v, w)$  is the amplitude attenuation as a function of ray direction and  $\Phi(u, v, \xi, \zeta, z)$  is the phase of a ray with direction  $(u, v)$  as it propagates the object space, and  $w = \sqrt{1 - u^2 - v^2}$ . The domain of integration,  $D$ , is the space of all ray directions leaving  $Q$  and reaching the lens plane. Here the lens plane coordinates  $(\xi, \zeta)$  are mapped to the  $(x, y, z)$  coordinate system. To be consistent with the light ray discussion, the lens plane is located at  $z = z_2$  where  $z_2 > z_1$ . Then  $\xi = \alpha(z_1) + \alpha'(z_2 - z_1)$  and  $\zeta = \beta(z_1) + \beta'(z_2 - z_1)$ . Therefore the phase function,  $\Phi(u, v, \xi, \zeta, z)$  can be written in terms of  $(x, y, z)$  as

$$\Phi(u, v, x, y, z) = W(u, v, x, y, z) + n_{obj}[ux + vy + w(z - z_1)] \quad (17)$$

where  $W(u, v, x, y, z)$  is the optical pathlength of the ray as it propagates through the inhomogeneous object area, from  $z = z_0$  to  $z = z_1$ , and the linear terms represent the pathlength through the homogeneous medium with refractive index  $n_{obj}$ . The phase contribution of any one ray,  $(u_i, v_i)$  [Fig. 5] at  $P_0$  is the optical pathlength from  $Q$  to  $P_i$ .  $P_i$  is the point where a line from  $P_0$ , perpendicular to ray  $(u_i, v_i)$ , intersects the ray  $(u_i, v_i)$ . Since each ray  $(u_i, v_i)$  represents a locally planar wavefront normal to the ray, the optical pathlength along that plane, and thus a line on that plane, is constant. As shown in Chapter XII of Kline, et. al.<sup>16</sup> the above integral can be solved asymptotically by performing a Taylor series expansion about  $P_0$ . The first order approximation of the field, from the resulting expansion, is

$$U_1(\xi, \zeta) = \frac{A(u_0, v_0, w_0)}{\sqrt{\Phi_{uu}\Phi_{vv} - \Phi_{uv}^2}} \exp [ik\Phi(u_0, v_0, \xi, \zeta, z_2)] \quad (18)$$

where the subscripts indicate derivatives evaluated at  $P_0$ . The term in the denominator is the local radius of curvature of the phase function at  $P_0$ . Here we ignore diffraction effects due to rays intersecting the lens aperture. This simplification is justified if objects are small compared to the field of view of the lens and located close to the center of the field. This approximation also assumes that no caustics occur in the region of the object. This assumption can be relaxed, if need be, and additional fields due to caustics can be included.<sup>16</sup> Another important assumption is that the optical pathlength of rays from object points to the lens exit plane is large enough that wavefronts approach spherical, i.e.

$$\left| \frac{U_1}{\sqrt{\Phi_{uu}\Phi_{vv} - \Phi_{uv}^2}} \exp [-ik\Phi] - A(u, v) \right| \leq \epsilon \quad (19)$$

such that  $\epsilon$  is small. We validated this assumption by tracing a number of rays with different  $(u, v)$  values and tested the sphericity of the resulting wavefronts. Some results for one test specimen are shown in Fig.6. In our simulations, with the objective working distance approximately  $100\lambda$ ,  $\epsilon$  ranged between  $[1e - 9, 5e - 8]$ . Accordingly, the wavefronts do approach spherical in the local vicinity of the lens plane point and therefore we justify using this approximation. In the case that more accurate simulations are required, additional terms of the Kline-Luneberg series can be incorporated into the computation.

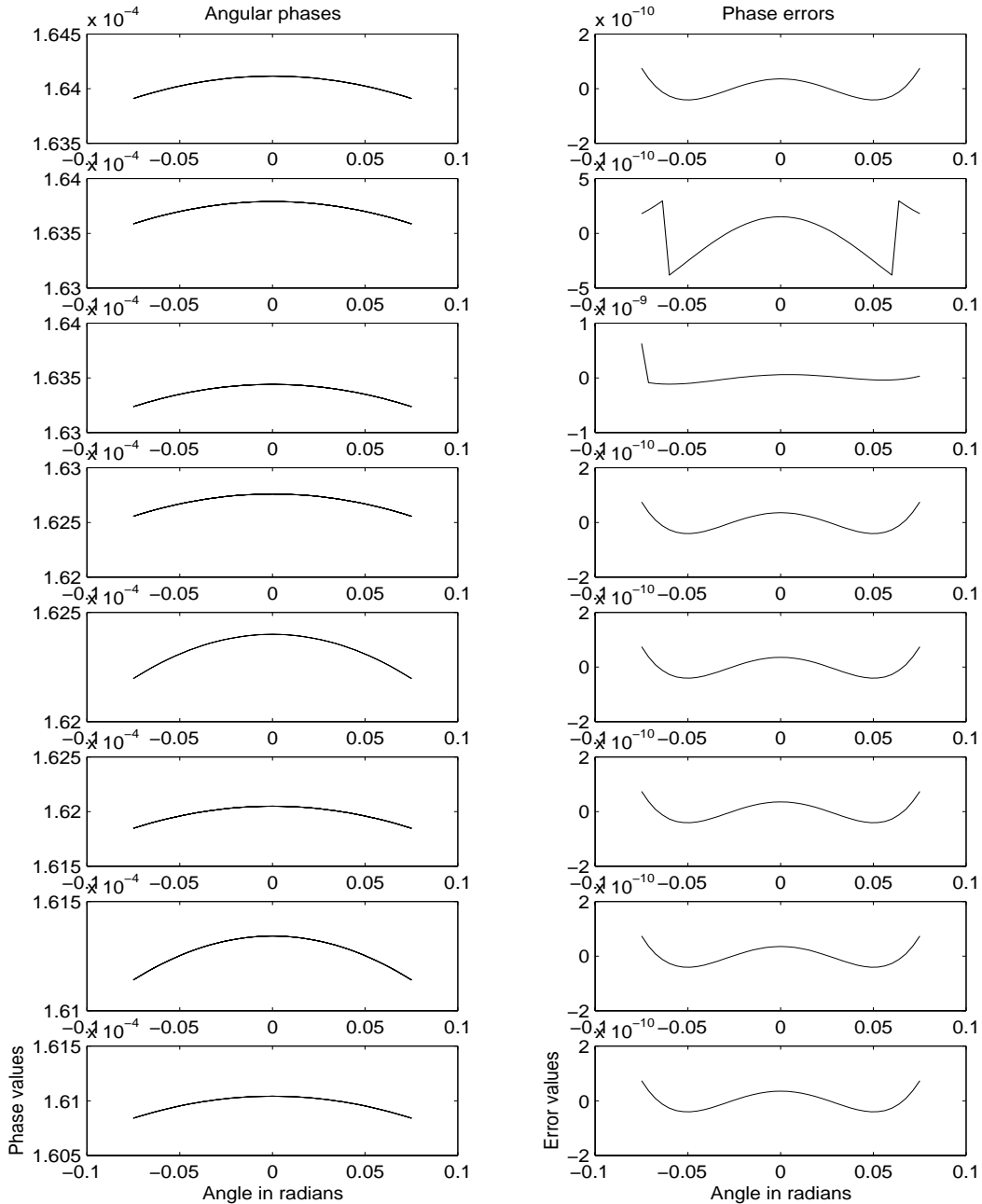


Fig. 6. Plot of phase values encountered at example object from different object points. The plots in the left column show phase retardation as the  $u$  component of the ray direction is changed by the amount shown. Each plot emanates from a different object location. From top to bottom, the object locations are farther away from the lens plane. particular object location. Though, it is hard to differentiate, each plot has two curves: the actual numerically calculated phases and the closest fit spherical curve. The plots in the right column show the errors between the calculated phases and the spherical curve for each respective plot in the left column.

The estimated curvature is used to determine the intensity distribution at the image plane. The lens transforms the field to a spherical wavefront converging to a point in the image space. The point of convergence, referred to as the image point, is determined by the lens law  $\frac{1}{d_o} + \frac{1}{d_s} = \frac{1}{f}$ , where  $d_o$  is the estimated radius of curvature and  $f$  is the lens focal length. The curvature of the wavefront at the lens entrance plane, and the lens focal length completely determine  $d_s$ , the distance from the lens exit plane to the image point. The field in the vicinity of the image point is represented by

$$U_{img}(x_{img}, y_{img}, z_{img}) = \frac{-i}{2\lambda} \int \int_{\alpha} \frac{A_o \exp[-ik(r_s - r_i)]}{r_i} \cos[\vec{n}_{\alpha} \cdot \vec{r}_s] - \cos[\vec{n}_{\alpha} \cdot \vec{r}_i] dS \quad (20)$$

where

$$r_i = \sqrt{(x_{img} - \xi)^2 + (y_{img} - \zeta)^2 + z_{img}^2}, \quad (21)$$

$$r_s = \sqrt{(x_s - \xi)^2 + (y_s - \zeta)^2 + z_s^2}, \quad (22)$$

$A$  is the entire aperture surface,  $\vec{r}_s$  is a vector from a point on  $A$  to the image point  $(x_s, y_s, z_s)$ ,  $\vec{r}_i$  is a vector from the point on  $A$  to  $(x_{img}, y_{img}, z_{img})$ ,  $r_i$  is the length of  $\vec{r}_i$ ,  $r_s$  is the length of  $\vec{r}_s$  and  $\vec{n}_{\alpha}$  is the normal to plane containing the lens aperture. Points on the aperture are denoted by  $(\xi, \zeta)$ . To see the relation between the above equation and Eq. 11 one substitutes  $U_2(\xi, \zeta) = A_o \exp[-ikr_s]$ .  $\cos[\vec{n}_{\alpha} \cdot \vec{r}_s] - \cos[\vec{n}_{\alpha} \cdot \vec{r}_i]$  is a slowly varying direction term which is ignored. According to the derivation by Gibson, et.al.,  $U_{img}$  can be approximated by

$$U_{img}(x_{img}, y_{img}, z_{img}) = \frac{ikA_o a^2}{r_{img}} \exp ik(r_{img} - d_i) \int_0^1 J_0(\rho\omega_1) \exp i\rho^2\omega_2 \rho d\rho \quad (23)$$

where

$$\omega_1 = ka \sqrt{\left(\frac{x_{img}}{r_{img}} - \frac{x_i}{r_i}\right)^2 + \left(\frac{y_{img}}{r_{img}} - \frac{y_i}{r_i}\right)^2}, \quad (24)$$

$$\omega_2 = ka^2 \frac{r_{img} - r_i}{2r_{img}r_i}, \quad (25)$$

and  $a$  is the radius of the lens aperture. Consequently, given the amplitude of a wavefront from a particular object point, and its local curvature at the lens entrance plane, the corresponding contribution at different points of the image space is given by the above equation.

## 4. Polarized Light Propagation

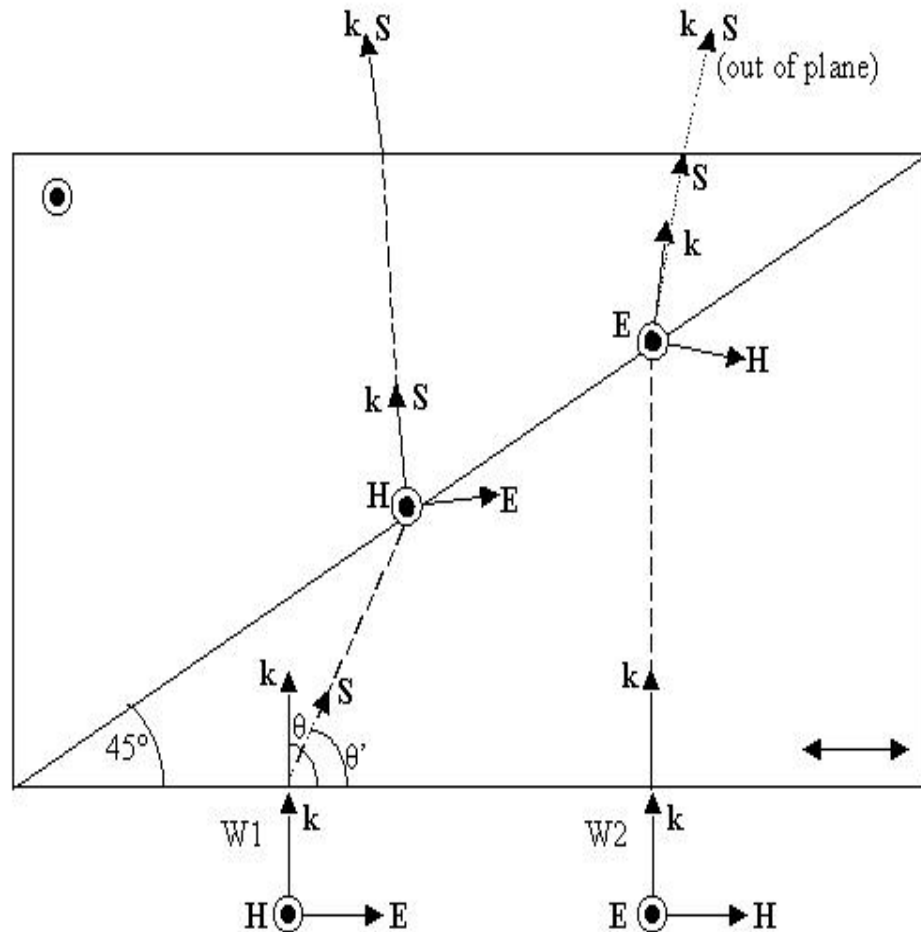


Fig. 7. Two possible paths of perpendicularly polarized fields are shown as they would propagate through the prism. For ease of illustration, the rays for each field originate at different source points.

In DIC optics, the differential separation between the two wavefronts occurs because the Wollaston (or Nomarski) prism introduces a different phase delay to the two perpendicularly polarized field components. Therefore, to determine the proper phase biases, we use

polarization ray tracing techniques<sup>4,23</sup> and propagate rays through the prism components. The Wollaston prism is made up of two wedges of a uniaxial birefringent crystal, such as quartz or calcite. The refractive index of such a crystal is different depending on whether the field is propagating perpendicular or parallel to its axis of symmetry. If the propagation vector of the field has a component in the direction of the axis of symmetry, the refractive index is a function of the angle between the propagation direction and the crystal's axis. By incorporating this property of uniaxial crystals, we trace ray paths through the prism and calculate the phase difference between the two polarized field components.

In uniaxial crystals the effective refractive index of a propagating field is different if the E-field of the wave lies in the principal section of the crystal than if it is normal to the principal section. The principal section is defined as the plane containing the crystal axis and the wave normal vector,  $\vec{k}$ . A wave with this polarization is called an extraordinary wave. In addition, for extraordinary waves, the ray vector  $\vec{S}$ , indicating the direction of energy flux, is no longer coincident with the wave normal vector  $\vec{k}$ . If the E-field of the wave is normal to the principal section, it is called an ordinary wave and behaves as it would in an isotropic medium. The refractive index for extraordinary waves with the E-field aligned parallel to the crystal axis is  $n_e$  and for ordinary waves the refractive index is  $n_o$ . If an extraordinary wave has an E-field not exactly parallel with the crystal axis, its effective refractive index  $n_{effec}$  satisfies the following equation,

$$\frac{1}{n_{effec}^2} = \frac{\sin^2\theta}{n_e^2} + \frac{\cos^2\theta}{n_o^2} \quad (26)$$

where  $\theta$  is the angle between  $\vec{k}$  and the crystal axis in the principal section. For extraordinary waves, the angle,  $\theta'$ , between the ray vector  $\vec{S}$  and the crystal axis satisfies the following equation

$$\tan\theta' = \frac{n_o^2}{n_e^2} \tan\theta \quad (27)$$

When a wave with the E-field lying in the principal section intersects such an uniaxial medium, the wave normal vector  $\vec{k}$  and  $n_{effec}$  are mutually dependent. Therefore, one must

solve a quadratic equation to calculate the refracted  $\vec{k}$  and  $n_{effec}$ . A method for doing so is discussed in Trolinger, et.al<sup>24</sup>.

By considering each wedge of the Wollaston prism as a uniaxial quartz crystal with the crystal axis in each wedge orthogonal to each other, we can trace rays representing the two polarized fields and obtain the corresponding phase delays.[Fig. 7] We assume that the first field (W1) has its E-field component parallel to the crystal axis of the first wedge. The second field (W2) has its E-field direction parallel to the crystal axis of the second wedge. At the boundary of the first wedge, W1 is an extraordinary wave, while W2 is an ordinary wave. To propagate W1 through the first wedge, we need to calculate two separate vectors  $\vec{k}_1$  and  $\vec{S}_1$ . When  $\vec{S}_1$  intersects the boundary between the first and second wedges,  $\vec{k}_1$  and  $n_{effec}$  is used in Snell's refraction law to calculate the refracted wave normal vector. At this point, this wave behaves as an ordinary wave and the ray and wave vectors are coincident. Wave W2 propagates through the first wedge as it would in an isotropic medium with refractive index  $n_o$ . At the intersection of the boundary between the first and second wedges, it now behaves as an extraordinary wave with a  $n_{effec}$  and separate  $\vec{k}_2$  and  $\vec{S}_2$ . At the last boundary, using Snell's laws and each wave normal vector for W1 and W2, the refracted wave normal vector can be calculated for each wave. After this point, the wave normal vector and ray vector for each wave are coincident. As is evident from the prism structure, the phase bias between the two waves changes transversely across the prism. Therefore, by translating the prism microscopists achieve an optimal bias for each specific specimen.

## B. Illumination Model

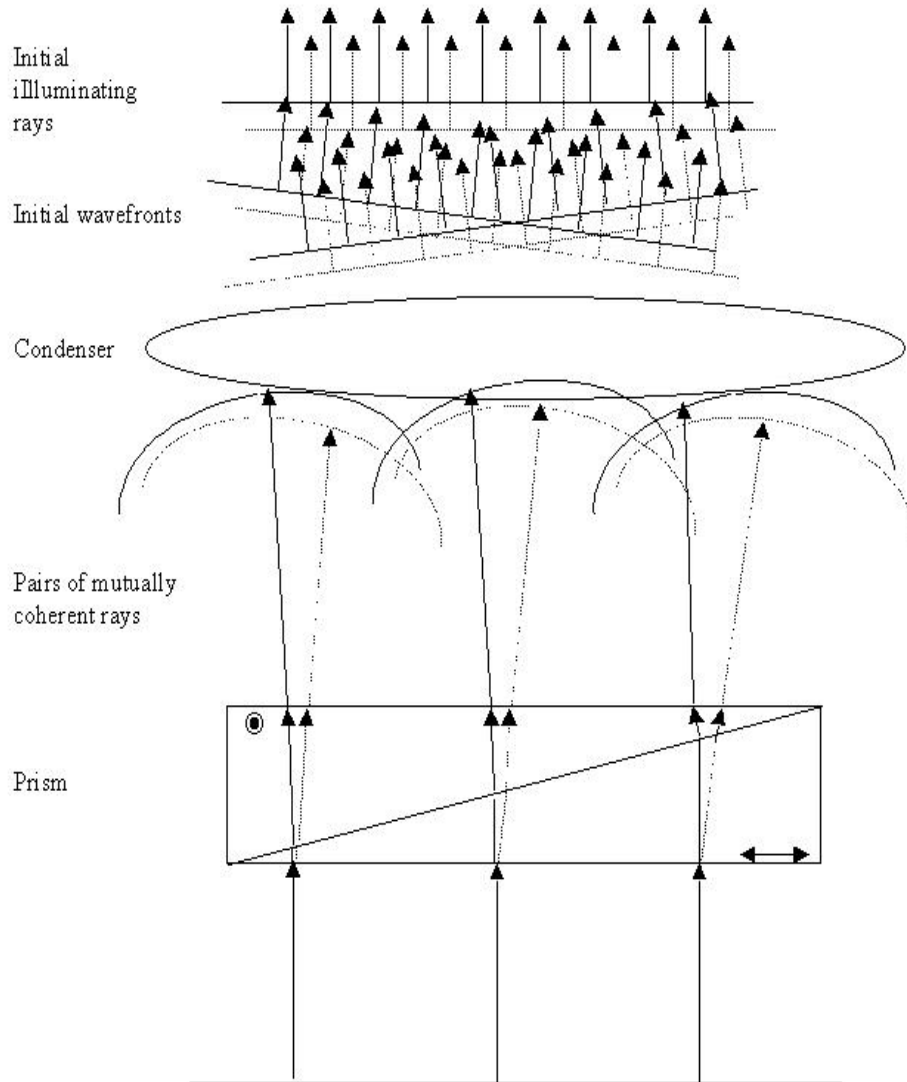


Fig. 8. Illumination model: The schematic depicts three point sources in the aperture, each resulting in two orthogonally polarized wavefronts which reach the condenser lens. The condenser transforms the wavefronts into planar wavefronts with different directions. Illuminating rays in our model originate at sampled points along these wavefronts.

The light illuminating the object in DIC optics is partially coherent due to the finite size

of the condenser aperture. The light in the microscope originates in an incandescent lamp, filtered to a moderate bandwidth. An auxiliary lens forms an image of the light source on the condenser's pupil. Due to the point spread function of the auxiliary lens, light emitted from neighboring points in the pupil is phase-correlated. Points on the condenser pupil which are closer than the radius of the auxiliary lens' point spread function will have correlated phases. If the condenser aperture were closed down to a point, then a perfectly coherent planar wavefront would emerge from the condenser lens. A point aperture is impractical due to its vanishingly small light flux resulting in a low signal to noise ratio in the image. Thus the finite extent of the condenser pupil gives rise to partial coherence in the image energy distribution.

In our model, rays representing light from sampled points in the condenser pupil, with appropriate bias due to the prism, provide the initial illumination on the object. Initially, a set of rays originating from sampled points in the condenser pupil are traced through the prism. The amplitude contributions in the image from each one of these initial rays is added incoherently. Physically, this implies that the sampling period across the pupil is larger than the point spread of the auxiliary lens, and therefore the points are not phase correlated. Each one of these initial rays results in two sets of parallel rays impinging on the specimen. Each set of parallel rays represents a discretely sampled wavefront, with one set having a field polarization orthogonal to that of the other set of rays. [Fig. 8] The amplitude contribution of these two parallel sets of rays is added coherently. At present we only attribute one specific wavelength to the rays, ignoring the finite bandwidth of the light. In a DIC microscope, the Wollaston prism is aligned with respect to the condenser pupil such that uniform interference results. Thus rays of all directions from a particular pupil point encounter the same phase retardation through the prism. Consequently, we propagate only the axial ray from each point in the condenser pupil through the prism, using the polarization ray-tracing equations. The difference in phase between rays representing the two orthogonal field polarizations, is the phase bias between the two sheared wavefronts. This computation can be done once for a given prism specification and remains invariant

for all simulations thereafter. Effectively, the condenser lens performs a Fourier transform. By the spatial shift theorem of the Fourier transform, the translation of a function  $g(x, y)$  is a phase shift in its frequency representation  $G(f_x, f_y)$ ,

$$\mathcal{F}[g(x - a, y - b)] = G(f_x, f_y) \times \exp[-i2\pi(f_x a + f_y b)]. \quad (28)$$

Therefore, the direction of the light rays is determined by the displacement of the corresponding source point from the origin.

The illumination system is modelled by four parameters: the radius of the condenser pupil, the shear direction and magnitude, and the phase bias. The condenser aperture size is determined by the numerical aperture of the lens. Fig. 9 shows differences in simulated images of the same object with different condenser radii. As can be seen, a larger aperture results in higher axial resolution than a smaller aperture. When comparing the intensity profiles of the two sets of images, [Fig. 10] one observes that the object's in-focus features are sharper in the images simulated with a larger aperture than with a smaller aperture. This is consistent with theory suggesting that higher object frequencies are probed with a larger aperture radius than with a smaller one, and therefore both axial and transverse resolution is improved. In contrast to the condenser aperture, the shear amount is usually a fixed property of the optics. The magnitude of the shear is established by the manufacturer of the prism and is usually on the order of the objective lens' Rayleigh resolution. Each objective lens will have a prism specifically designed for it. The phase bias is set experimentally by the user to obtain best contrast. In our experiments, we have determined the phase bias for selected prisms by interferometry and measured prism offset for each acquired data set.

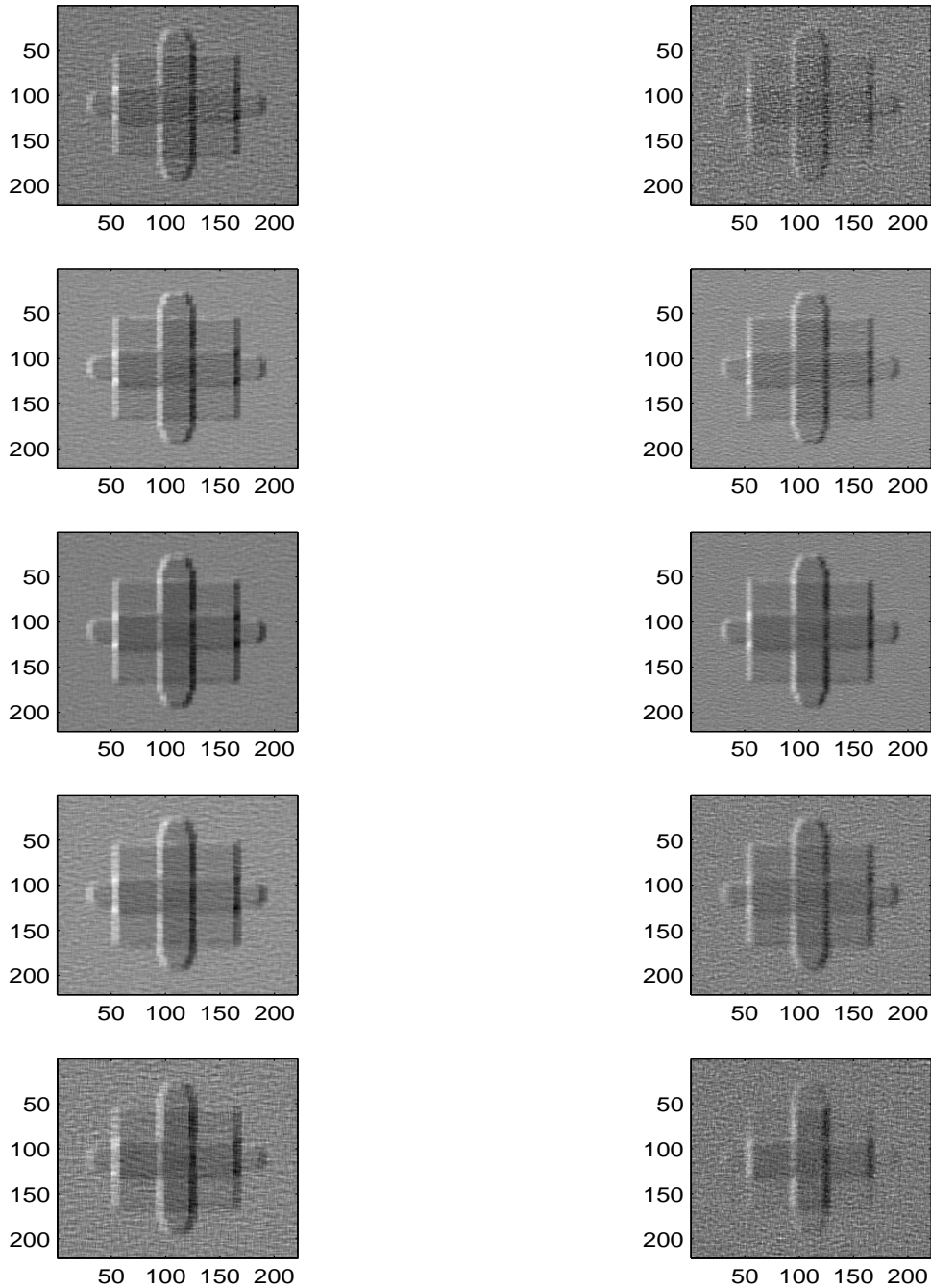


Fig. 9. Simulated images of two differently sized condenser apertures. The left column has been simulated with a small aperture and the right column with a larger aperture radius. The axial resolution is higher in the right set, since the images defocus over a shorter axial distance. Plots in the subsequent figure compare lateral resolution. Images are ordered from top to bottom, with a .04 micron spacing between each image.

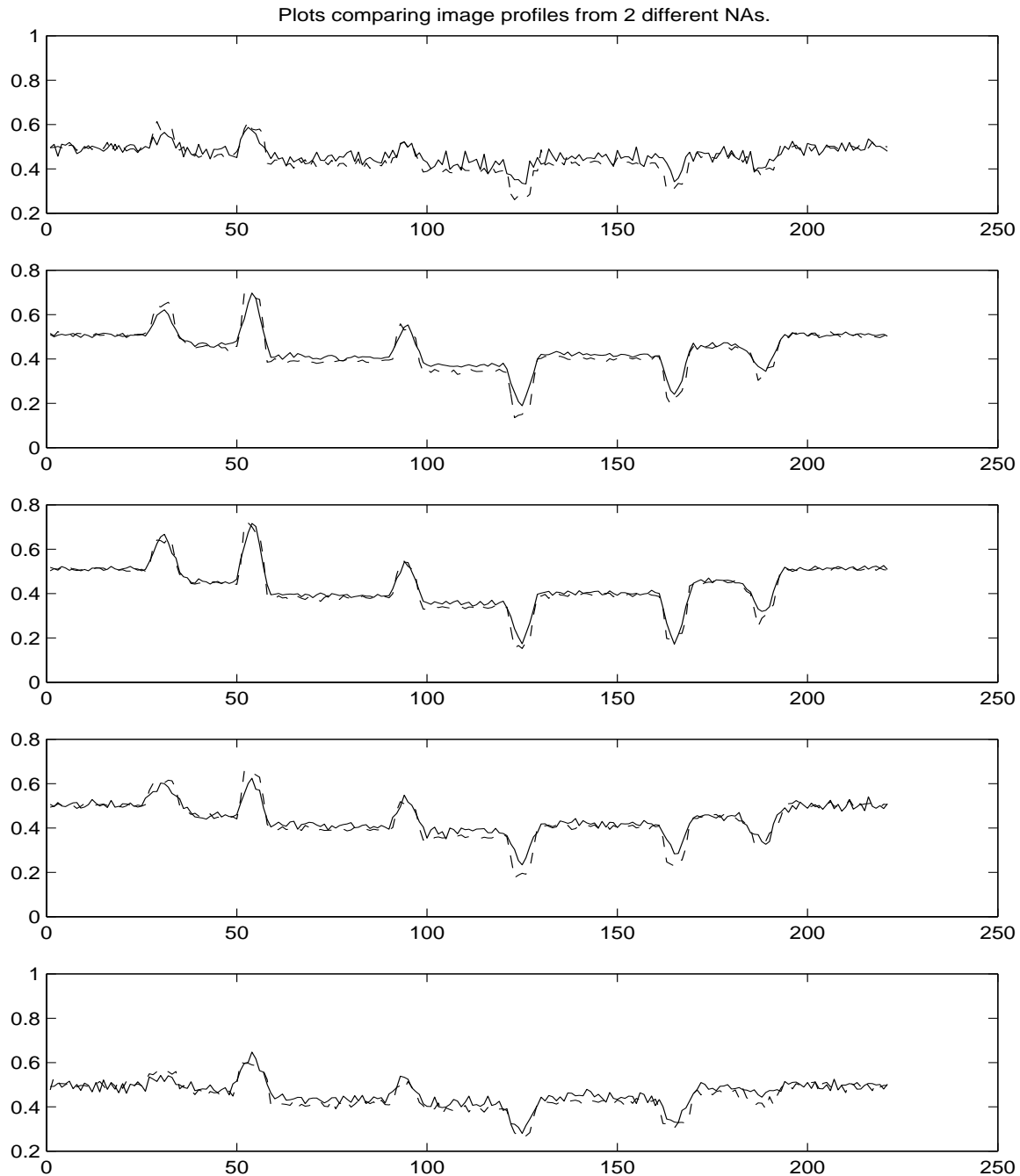


Fig. 10. Intensity profiles across simulated images in the previous figure. The dash-lined plots are from the images simulated with a small aperture and the solid-lined plots are from the images simulated with a larger aperture radius. The peaks of the dash-lined plots are wider than the solid-lined plots, especially apparent in the second and third plots. Images are ordered from top to bottom, with a .04 micron spacing between each image.

### C. Light Ray Implementation

Based on known properties of the illumination, a set of parallel rays is initialized at the condenser exit pupil with phase and amplitude polarization determined by the ray trace through the prism. In our model, each ray contains the local polarized amplitude polarization, propagation direction, and phase. The local coordinate system at each ray [Fig. 3] consists of the propagation vector  $\vec{k}$  and two orthogonal vectors,  $\vec{p}$  and  $\vec{q}$ , in the plane perpendicular to  $\vec{k}$ . The polarized field amplitude can be represented by decomposing the field along two orthogonal directions,  $\vec{p}$  and  $\vec{q}$  both of which are perpendicular to the propagation vector  $\vec{k}$ . Each vector is weighted by a complex scalar coefficient, which is the relative phase of the corresponding field components. The complex coefficients of the polarized electric field,  $E^p$  and  $E^q$ , are the components of a Jones vector. Therefore,

$$\vec{E} = \begin{bmatrix} E^p \\ E^q \end{bmatrix} = \begin{bmatrix} E_0^p e^{i\phi^p} \\ E_0^q e^{i\phi^q} \end{bmatrix} \quad (29)$$

represents the polarization state of a coherent wave. Here  $E_0^p$  and  $E_0^q$  represent the magnitude of the p- and q-components of the local electric field, respectively.  $\phi^p$  and  $\phi^q$  represent the phases.

As rays are traced through the object, the object's phase retardation is incorporated into  $\phi^p$  and  $\phi^q$ . Therefore, if the  $\vec{p}$  polarization direction has a  $\Delta\phi_{bias}$  phase bias with respect to the  $\vec{q}$  polarization direction,  $\phi^p = \phi_{obj}(\vec{x} + \vec{v}_s) + \Delta\phi_{bias}$  and  $\phi^q = \phi_{obj}(\vec{x} - \vec{v}_s)$ . These correspond to  $U_{obj}^1$  and  $U_{obj}^2$  in Eq. 4. The p and q polarization vectors are initially aligned with the  $x$ - and  $y$ -axis. Thus they are also aligned with the crystal axis of the wedges of the first prism. As the rays propagate through the object, the p and q vector directions rotate accordingly. After the lens transform, the vectors are aligned with the  $x_{img}$ - and  $y_{img}$ -axis. Subsequently, only the amplitude contributions projected onto those directions are relevant and therefore stored.

#### D. Object Model

The specimen model consists of a 3-D grid of voxels, extending over the entire object space. Each voxel, indexed by  $[i, j, k]$  contains a refractive index value and a gradient value sampled from a continuous distribution. The discretely sampled values are

$$n[i, j, k] = n(i\Delta x, j\Delta y, k\Delta z)$$

$$\nabla n[i, j, k] = \nabla n(x, y, z)|_{x=i\Delta x, y=j\Delta y, z=k\Delta z}$$

where  $n(x, y, z)$  is the continuous distribution,  $\nabla$  indicates the gradient operation and  $(\Delta x, \Delta y, \Delta z)$  is the grid resolution. Typical grids are square with a resolution of  $.01\mu\text{m}$ . The calculation of the three dimensional light rays use these discrete values. In Eq. 10, the values of  $n_{[i,j,k]}$  and its gradient  $\nabla n$  are used in the integration of the differential equations.

#### E. Prism Bias calculations

Based on polarization ray tracing techniques, the phase bias encountered by rays propagating through the prism can be written as a linear equation in x and y. Since the prism in DIC is aligned such that all rays from a particular point on a reference plane encounter the same phase, only the location of the ray on that plane is needed. For the first prism, the reference plane is the condenser pupil plane, and for the second prism, the reference plane is the front focal plane of the objective. Therefore, calculating the phase bias through the second prism only requires calculating the intersection point of a ray through the front focal plane of the objective. The phase calculations account for the distance between the reference plane and the prism boundary.

## F. Image Intensity Calculations

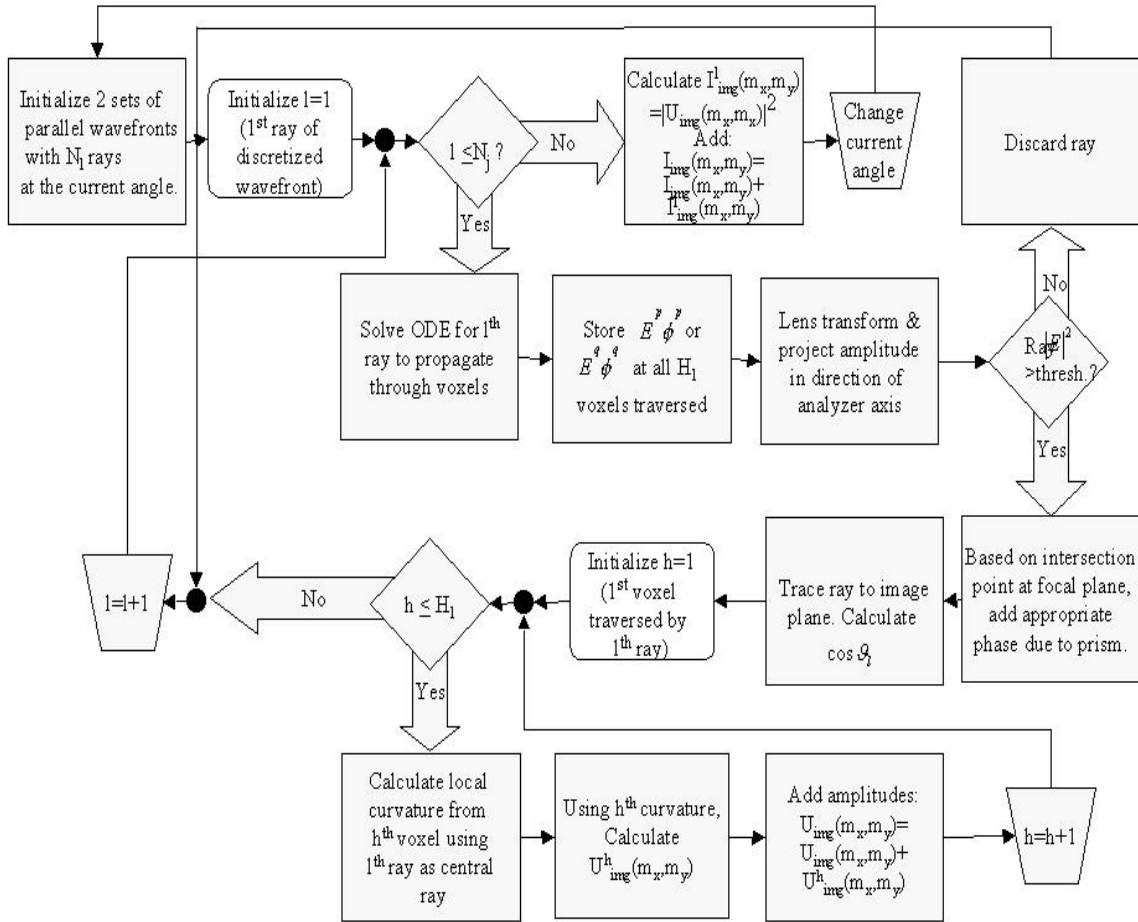


Fig. 11. Flowchart showing all the calculations that are made by our model in order to simulate DIC intensity images.

During each simulation, rays initialized at the condenser aperture, are traced through the object all the way to the image space. A flowchart shows all calculations performed in the model. [Fig. 11] Upon entering the object the ray path is found by solving the initial-valued set of differential equations (Eq. 9). The arc-length of the resulting three-dimensional curve weighted by the refractive index values of the traversed voxels is the optical path-length, which in turn determines the phase along the curve. At all traversed voxels the phase

along the ray path to that voxel is recorded. Upon exiting the object, each ray is then transformed by the lens and enters the image space. At this point, the ray's amplitude polarization is projected onto the analyzer axis and the ray splits off into two rays with perpendicular amplitude polarization components. The intersection of the subsequent rays with the lens focal plane and its polarization determine the bias due to the second prism. After projecting the amplitude polarization onto the analyzer axis, we discard rays which do not have magnitudes greater than a preset threshold. This eliminates computations which would have insignificant effects on the image intensity. For each of the remaining rays which intersect the image plane, its polarization is recorded at the intersection point.

If diffraction effects are ignored, the image intensity can be represented by a phase and amplitude superposition from each ray. Assume the transfer function in Equation 6 is  $K(x, y, x_{img}, y_{img}) = \delta(x - M_x x_{img})\delta(y - M_y y_{img})$  where  $M_x$  and  $M_y$  represent the scaling and inversion by the lens. The resulting intensity at a pixel  $(m, n)$  with contributions from  $N_j$  rays having the  $j^{th}$  initial angle is

$$\begin{aligned}
 I_{m,n} &= \sum_{j=1}^J \left| \sum_{l=1}^{N_j} \cos \theta_l [E_l^p \exp(i\phi_l^p) + E_l^q \exp(i\phi_l^q)] \right|^2 \\
 &= \sum_{j=1}^J \left| \sum_{l=1}^{N_j} \cos \theta_l [(E_l^p \cos \phi_l^p + E_l^q \cos \phi_l^q) + i(E_l^p \sin \phi_l^p + E_l^q \sin \phi_l^q)] \right|^2
 \end{aligned} \tag{30}$$

where  $E_l^p$  and  $E_l^q$  are the polarized amplitude components.  $\phi_l^p$  and  $\phi_l^q$  are the respective phases.  $(m, n)$  is the discrete pixel location in the image plane on which  $(x_{img}, y_{img})$  fall. The maximum initial angle is determined by the numerical aperture of the condenser lens.

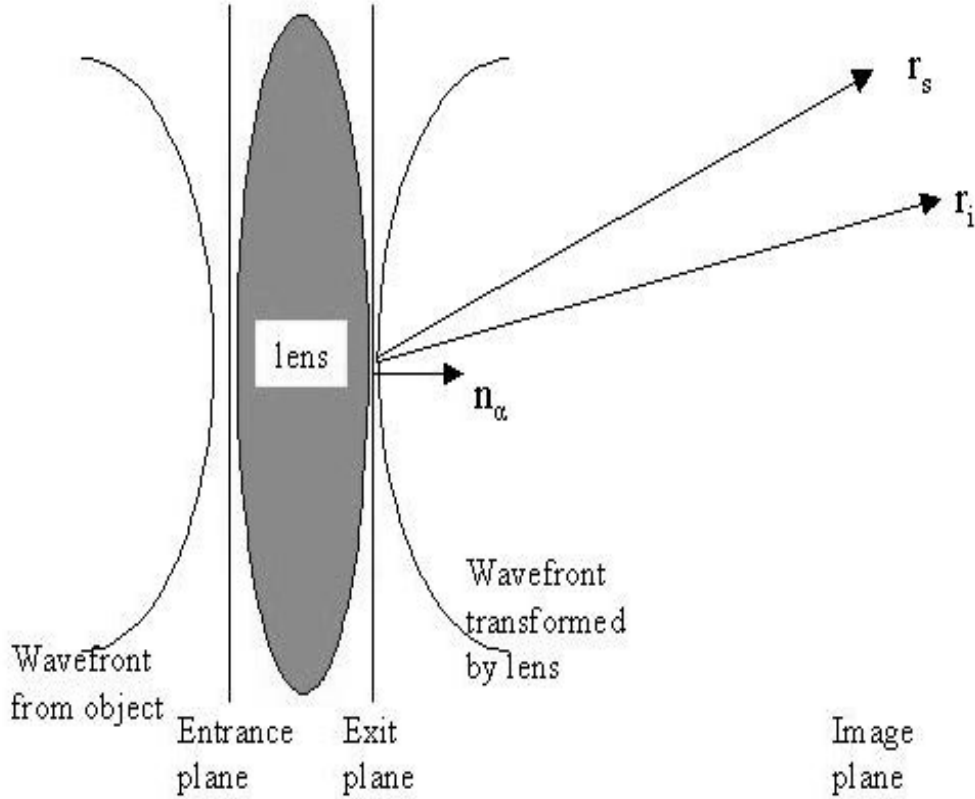


Fig. 12. Schematic of diffraction by the lens, corresponds to Eq.23. The wavefront from an object point is modelled as spherical which is transformed by the lens and converges at a point in the image space (image point). The vector from an aperture point to the image point is  $\vec{r}_s$ , the vector from the same aperture point to  $(x_{img}, y_{img}, z_{img})$  is  $\vec{r}_i$  and the vector normal to the aperture plane is  $\vec{n}_\alpha$ .

In reality, we approximate diffraction effects by the lens aperture and distortions by the object. Consequently, the above developments are modified so that energy from sources along each ray path contributes to more than one pixel. As a result of the inhomogeneities in the weakly absorbing specimen, the image plane receives a contribution of amplitude and

phase from all voxels in the ray path. Each contribution is computed as the diffracted field emerging from the specific voxel location. The wavefront's absolute phase is determined by the local phase of the ray recorded at that voxel. The field from the  $h^{th}$  voxel in the path of the  $l^{th}$  ray is  $E_{l,h} \exp[i\phi_{l,h}]$ . At each point in the image space,  $\vec{x}_{img}$ , we compute the amplitude contribution of each wavefront emerging from each voxel of the object. Thus the modified intensity is

$$I_{m,n} = \sum_{j=1}^J \left| \sum_{l=1}^{N_j} \cos \theta_l \left[ \sum_{h=1}^{H_l} K_{m,n,l,h} [E_{l,h}^p \exp(i\phi_{l,h}^p) + E_{l,h}^q \exp(i\phi_{l,h}^q)] \right] \right|^2 \quad (31)$$

where  $K_{m,n,l,h}$  is a complex weight determined by the curvature of the wavefront from the  $h^{th}$  voxel and the corresponding value of Eq. 23. A plot of a typical distribution of the diffracted field's magnitude to different planes in the image space from a single voxel point is shown in Figure 13. For efficient calculations during the actual simulation, we precompute the integral in Eq. 23 for a large sampled set of expected values of  $\omega_1$  and  $\omega_0$ . The numerically integrated solutions for these values are stored in a table. During simulation, we perform table lookups and interpolate the closest stored values.

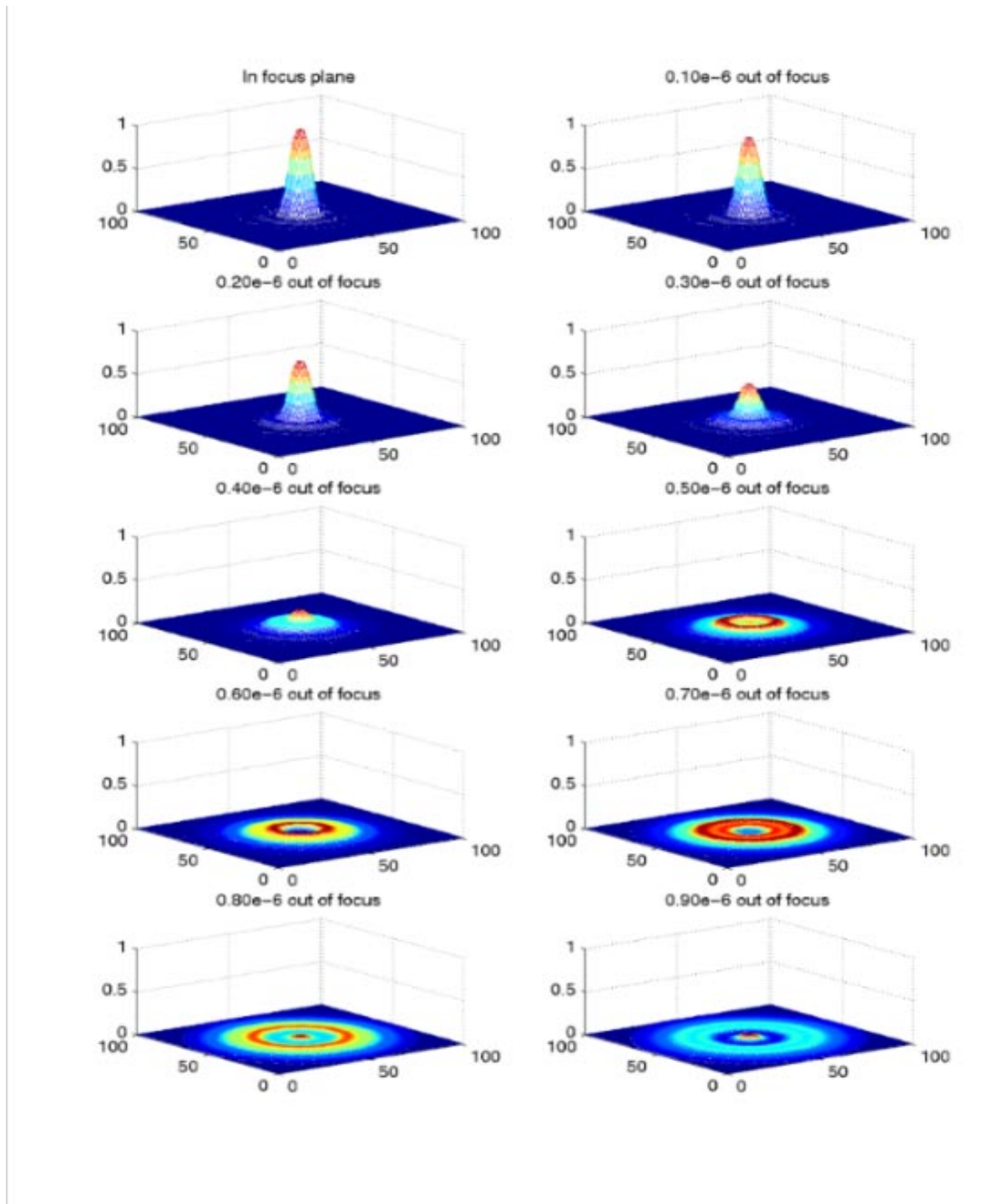


Fig. 13. Plots of amplitude magnitude distribution at different planes in the image space. The lens magnification for these plots was assumed to be 1X.

## 4. Experimental Validation of Model

### A. Prism Calibration Experiment

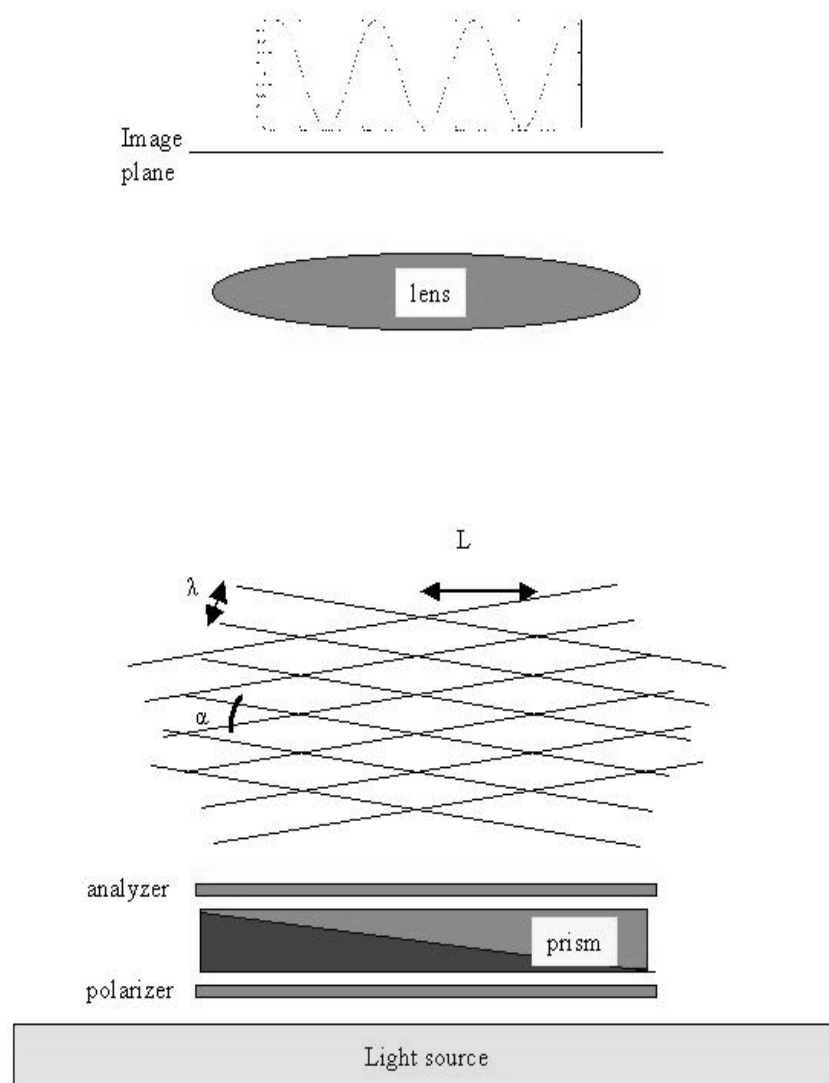


Fig. 14. Schematic of calibration experiment setup. The prism is placed between two crossed polarizers, on an extended light source, such as a fluorescent light table. The wavefronts that propagate through are modelled as planar with an angular separation denoted by  $\alpha$ . The camera (represented by the lens) records the resulting interference pattern.

As part of the calibration experiment, measurements were performed to quantify the bias between the two polarized wavefronts introduced by the Nomarski prism. The prism was placed between crossed polarizers and illuminated with light filtered by three narrowband filters of different wavelength ranges.[Figure 14] The polarizer-prism setup was placed on a white fluorescent light table, an extended light source. With the combination of the extended light source, polarizers and light filters, the illumination was approximated as planar waves. The resulting interference images were recorded using a CCD camera with a 35mm camera lens placed directly above the prism and polarizers.[Fig. 15]

Considering the geometry in Fig. 14, the angular separation can be written as

$$\alpha = 2 \arcsin \frac{\lambda}{2L} \quad (32)$$

where  $\lambda$  is the wavelength of light,  $L$  is the fringe separation in the interference image, and the angular separation is assumed to be small. The amount of phase bias between the two wavefronts varies from a minimum of zero in the center of the prism, to a maximum of  $\frac{\lambda}{2}$  at the brightest point in the pattern. The shear vector in the object space coordinates is  $\alpha f_c$ , where  $\alpha$  is computed above, and  $f_c$  is the focal length of the condenser lens. The measured prism parameters are shown in Table 1. The intensity plot along a line from each interference image is shown in Fig. 16. For each wavelength range, an effective separation angle is estimated and the interference patterns due to the estimated angle and real data are compared.

In subsequent experiments, the results of the bias measurements were used to calibrate the phase shift between the two wavefronts as the prism was moved past its central location. Before each experiment, the prism was positioned such that the phase bias was zero. Then it was translated to achieve the best contrast in the images, as is traditionally done by microscopists. Once the best translation was found, a plastic screw locked the prism translating mechanism. After the data was acquired, the prism was removed from its slot in the microscope, with the lock-screw still in place, and the translation from center was measured with a micro-meter. The corresponding phase was then obtained by looking up

the measured distance in the plots. [Fig 16]

Table 1. Calibrated Prism Parameters for 100X Objective.

Wavelength	Angular Separation	Shear
480 nm	.105618e-3 radians	.17215 microns
546 nm	.104582e-3 radians	.17046 microns
640 nm	.104310e-3 radians	.17003 microns

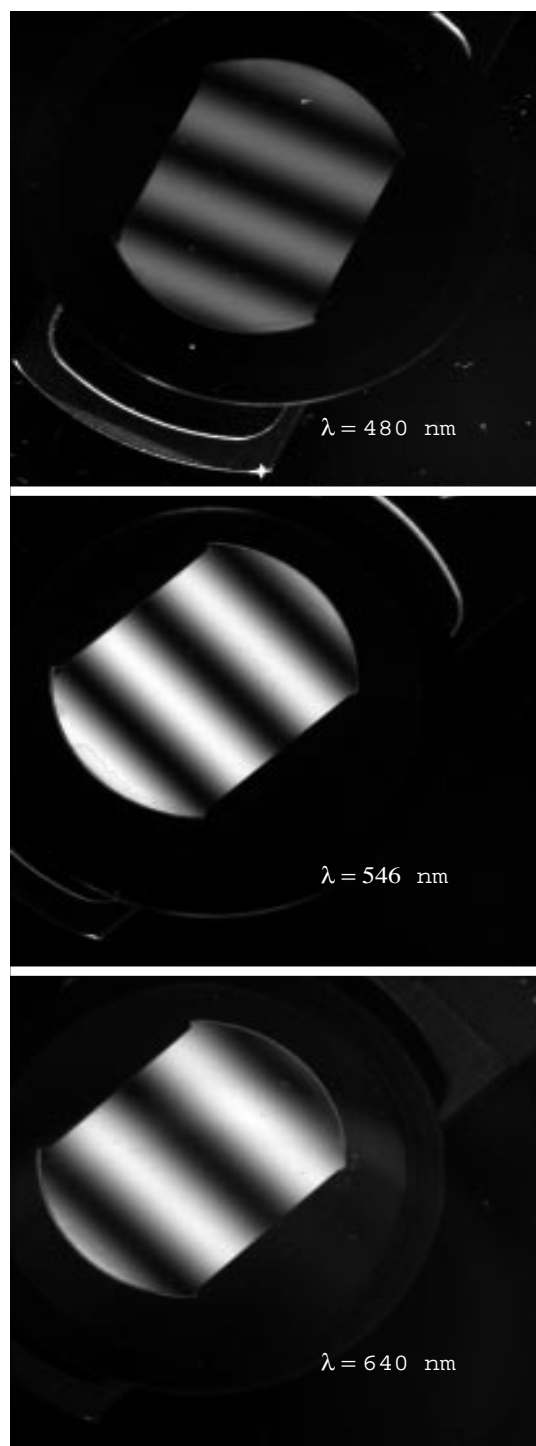


Fig. 15. Images of the prism's interference fringes taken by a CCD camera. The calibration setup is described in the text. In each case the light was filtered using a narrowband filter with center wavelength as shown above and approximately 20nm bandwidth.

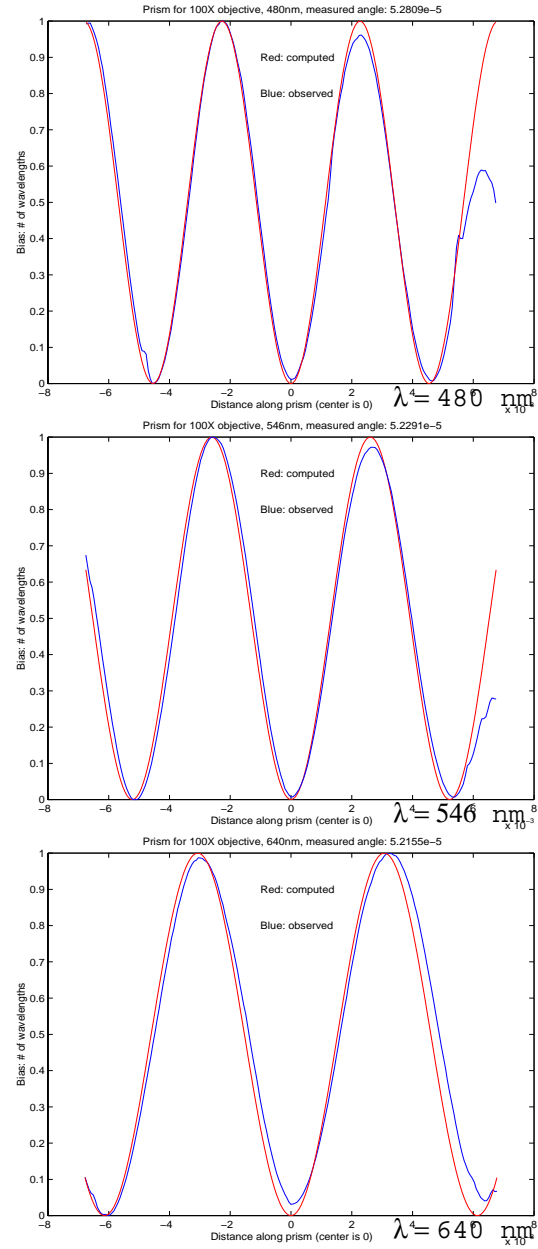


Fig. 16. Intensity plots from the images of the prism's interference fringes. In each case the angular separation between the planar wavefronts was estimated. An estimated interference plot, based on this estimated angle, was simultaneously plotted with the real data. The plots agree quite closely, especially in the central region of the prism which is of primary interest.

## B. Model Validation Experiments

Table 2. Specifications of the Plan Neofluar oil-immersion objective lens as reported by Zeiss, Inc.

Parameter	Value
Numerical Aperture	1.3
Magnification	100X
Focal Length	1.63 mm
Working Distance	0.06 mm
Pupil Diameter	4.2mm

To validate our model, we fabricated test specimens of known optical properties and structure. Two glass samples were created using photo-lithography and ion-milling. The milled distance was determined within a tolerance of 100 angstroms. The schematics of both the milled patterns are shown in Figure 17. The surface of a Corning glass wafer, such as the one we used, is assured to be optically flat and the optical properties (index of refraction, transmission, and absorption) are well-documented. The index of refraction for the glass is 1.53 (defined in light of 589.3 nm) and the absorption is 7% of light intensity (for light of wavelength 640nm) per 1mm of glass. The cavity was filled with an oil of refractive index 1.45. The experimental specimens were imaged using an inverted microscope (Zeiss Axiovert). The objective lens is a Zeiss Plan Neofluar, with the specifications shown in Table 2. The illumination was narrow bandpass filtered, with a passband centered around 480nm.

The real image data and simulated images of the first wafer are shown in Fig. 18. As can be seen, the simulations of this simple object matched well with the real data. The intensity peak at the object wall and its gradient agree with the real image. The second pattern was more complex and therefore the structure is not known as precisely. Due to imperfect milling, the virtual object model and real wafer were inconsistent, resulting in differences between the real and simulated images. This wafer required 3 millings and with each milling

the existing walls were smoothed out. So the deepest walls are also the least steep, which was qualitatively assessed from SEM images of the wafer. Each wall in our virtual wafer was assigned slopes estimated from measurements by a scanning touch probe. The probe tip was wider than some of the grooves and therefore it was not possible to accurately measure those slopes. In such cases, we modelled our virtual wafer walls with the best hypothesis based on design specifications.

The real image data from the actual wafer and the simulated images of the virtual model are shown in Figure 19. Also the walls of the actual wafer are not smooth and exactly parallel as are the walls of the virtual model, and this also contributes to differences in the real and simulated images. Artifacts appear in the actual data, such as double peaks when the edges are jagged and absent peaks when the object's edges are smoothed out. These irregularities are not modelled in the virtual object.

However, ignoring the artifacts due to irregularities in the object, it can be seen that the general characteristics of the real and simulated images agree. In both the simulated and real images, the correct features are in focus at the corresponding planes. The peak shape at the object walls do not match exactly, but the change in the peak as features come into/go out of focus is consistent. [Fig. 20] Fig. 21 contains the intensity profile across one image from the actual data and the profile of the corresponding simulated image superimposed. In doing so, the features in the images can be more easily compared. One observes that the peak heights in focused images match, and the corresponding out-of-focus peaks are consistently wider. The relative spacing between peaks also corresponds well. The comparison with the first wafer data shows that the image features which correspond to the refractive index's gradient can be reproduced in the simulation. The comparison with the second wafer data shows that the defocusing effects of the microscope can also be reproduced in the simulation. These properties are crucial if the computational model is to be used to reconstruct the object.

Since the computational model will be used in a reconstruction process, it is important that image features are consistent over the entire set. That is, features should be sharpest when in-focus and should be wider or more blurred in all other images. Also peak heights

should be consistent, relative to each other. That is, peaks corresponding to large changes in refractive index should have higher magnitudes than peaks corresponding to small changes. If these characteristics are properly simulated, and they have been shown to be consistent in our test cases, the computational model can be used for a reconstruction process. The discrepancies between actual data and simulated images, can be countered by additional constraints based on knowledge of the object during the reconstruction.

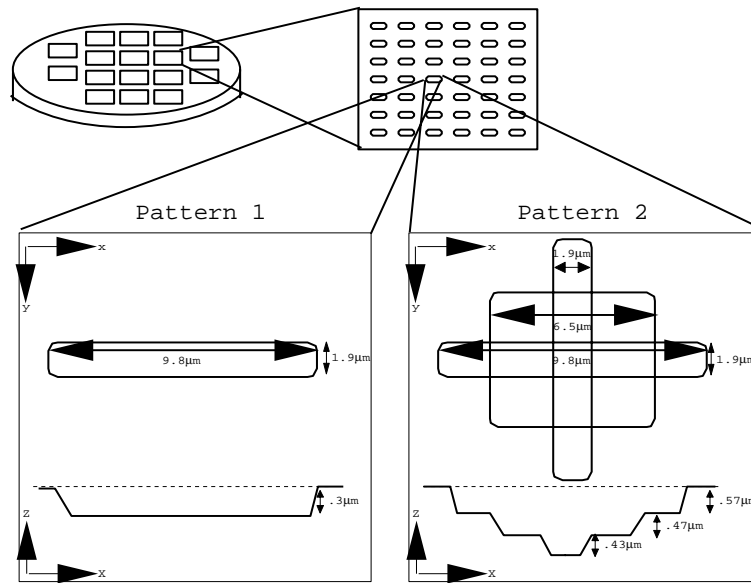


Fig. 17. Schematics of the two fabricated test wafers.

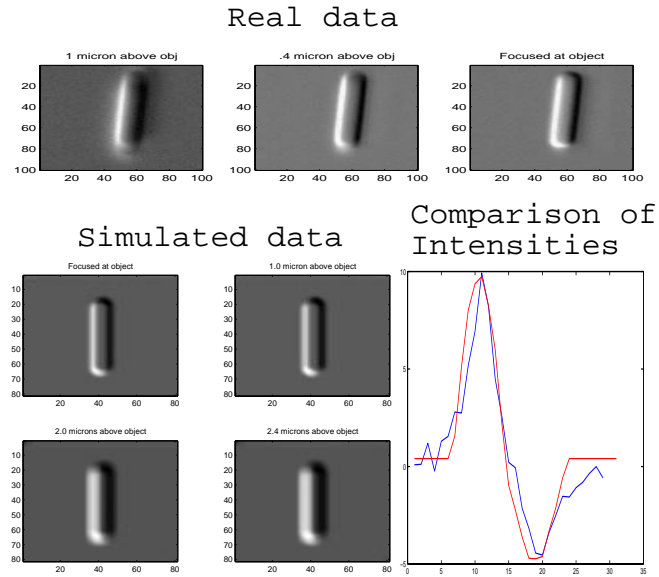


Fig. 18. The top row of images is real data of the glass wafer. Each image has a different object plane in focus with a .4 micron separation in Z between each image. The bottom left set of images is simulated data of corresponding planes (the fourth image's corresponding real image is not shown). The plot on the bottom right, compares the intensity distribution across one row of pixels in the first real and simulated images.

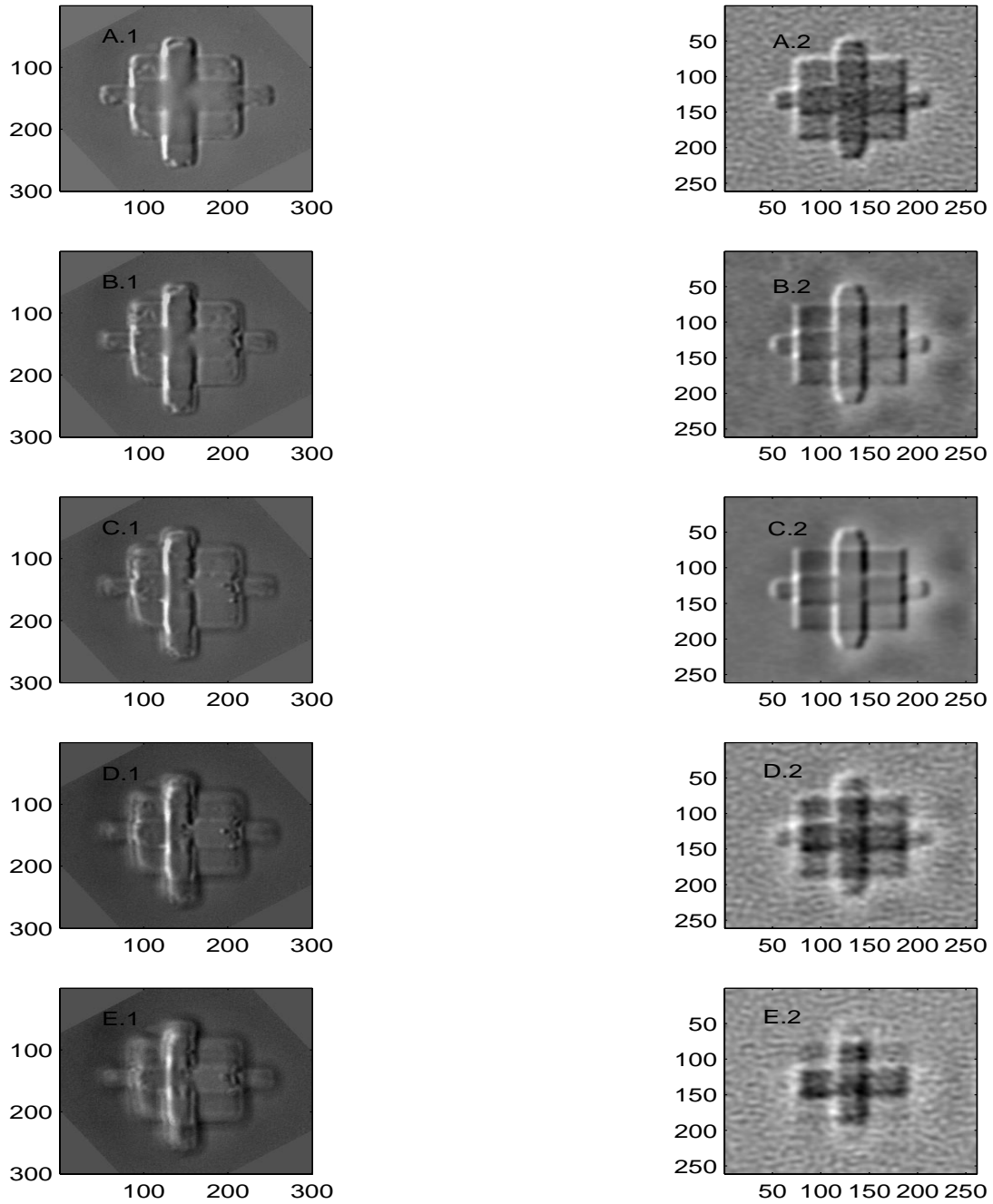


Fig. 19. The images in the left column are simulated images whereas the images in the right column are real data of Wafer 2. The data sets have a  $.1\mu\text{m}$  axial resolution. The top surface of the wafer etching is in focus in the first image of each column, with the etching oriented axially as shown in Fig.17. Each subsequent image is focused on a plane further down the object.

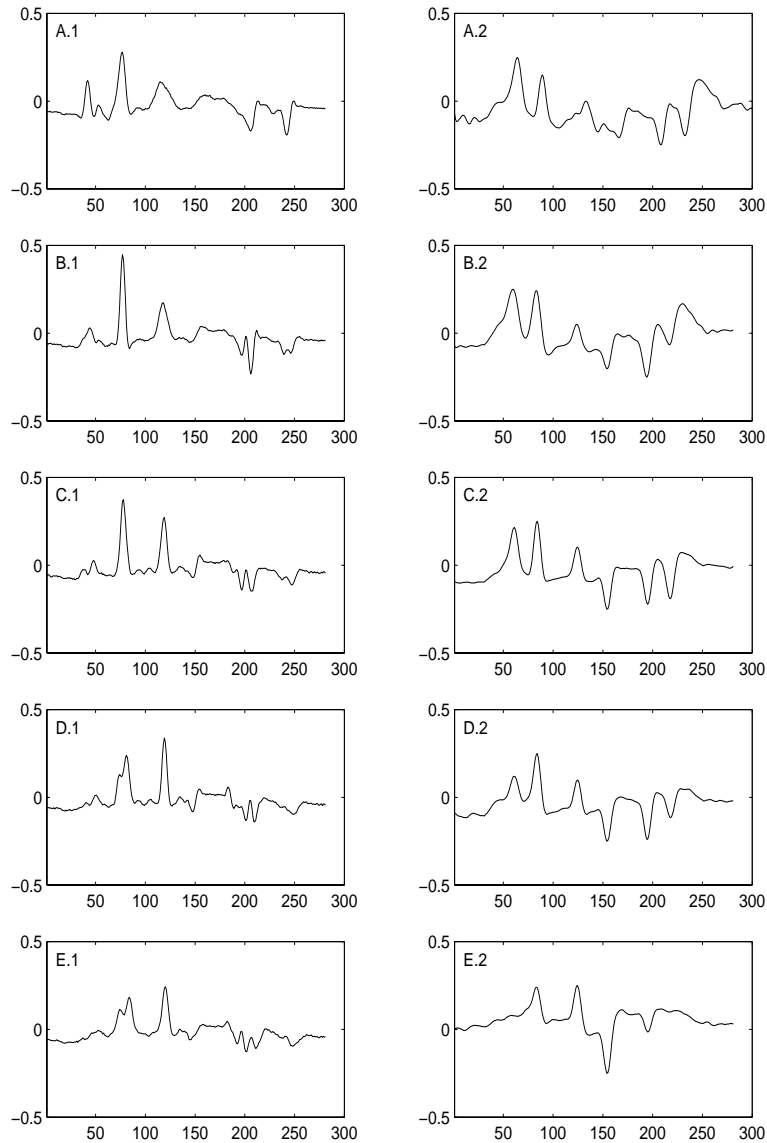


Fig. 20. Intensity plots of extracted lines from corresponding images in the previous figure. The relevant peaks have been numbered so that the relative heights can be compared between the real and simulated data. The relative heights of positive peaks should be compared since these correspond to the positive differential in the images. The other peaks correspond to the negative differential in the images. The change in peak heights as different object planes are focused on correspond in both data. For example, the leftmost peak is in focus in plots A.1 and A.2. and diminishes in D.1 and D.2. Whereas the third peak is lower in plots A.1, A.2, B.1 and B.2 whereas it is in focus in D.1, D.2, E.1 and E.2.

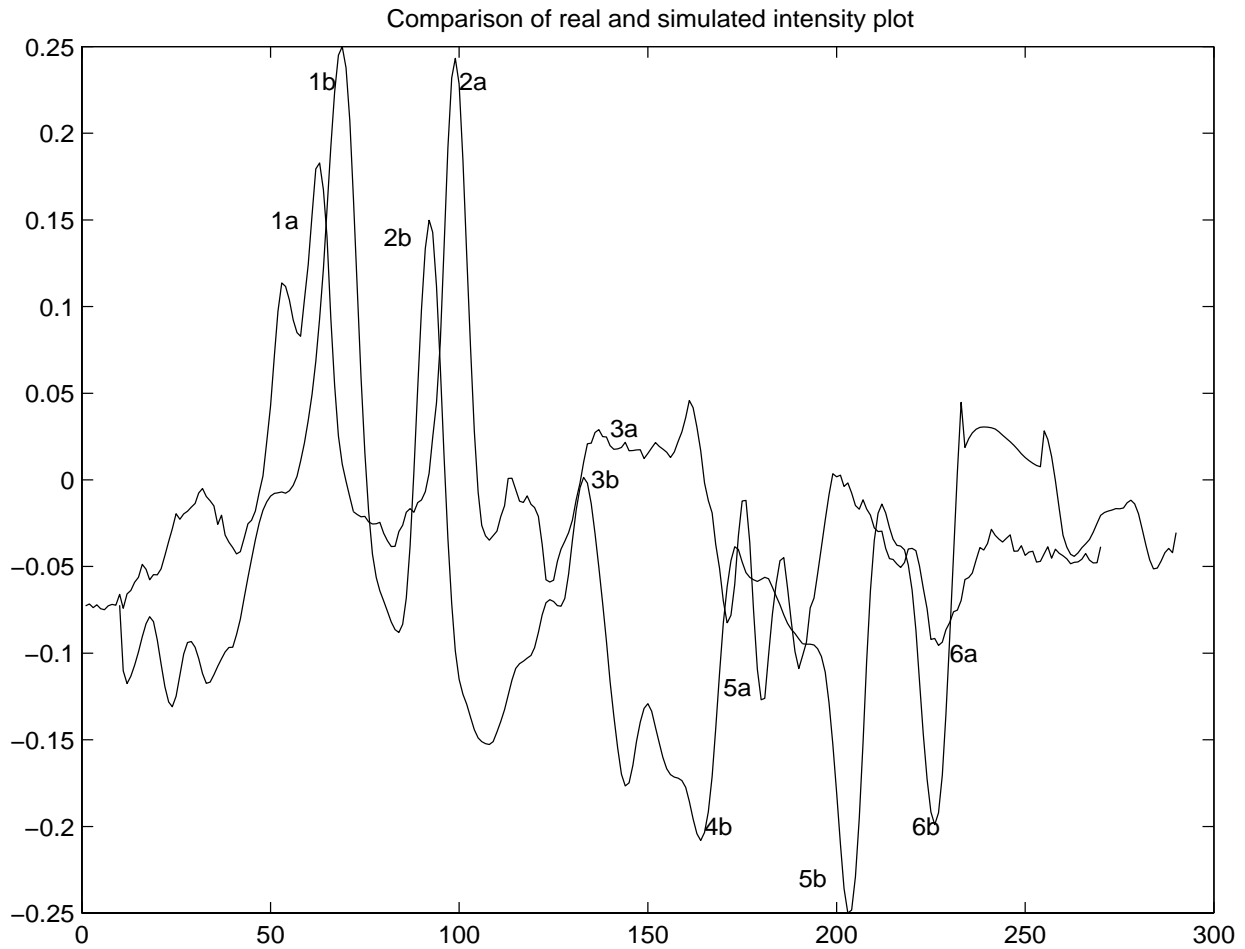


Fig. 21. Intensity profile of actual data and simulated images, superimposed to allow correspondences between images to be formed. The peaks labelled with the letter 'a' belong to the real data and the peaks labelled with the letter 'b' correspond to simulated data. As can be seen, most of the peak heights (peaks 1, 2, 3, 6) are comparable. The in-focus peaks (1, 2, 5, 6) have comparable widths, while the out of focus peak (3) is wider in both images. A distinct peak 4a is absent in the actual data indicating a smoothed out wall in the milling process. Peak 5 appears as multiple peaks in the real data which might be due to a jagged slope there.

## 5. Conclusion

Using physical principles of light propagation and computational techniques, we have developed a practical model of the image formation process in a DIC microscope. Our model can

handle inhomogeneous specimens for which analytical solutions have not been developed. We incorporate an approximation of distortions present in the image due to image inhomogeneities and explain the conditions under which these approximations are valid. Finally, we validate this model by comparing simulated data with images of actual specimens taken via a DIC microscope.

Currently, the above model is being used to reconstruct the refractive index distribution across an object volume. The model is the forward process in a non-linear optimization method. The object's refractive index distribution is projected onto a wavelet basis and the coefficients of these basis are estimated iteratively from coarse resolution levels to finer ones. By estimating the wavelet coefficients, rather than each discretely sampled refractive-index values, the dimensionality of the problem is drastically reduced and convergence occurs in fewer iterations. So far, only two dimensional objects have been reconstructed by considering one axial slice of the total object volume at a time. The extension to  $2\frac{1}{2}$  dimensions is trivially achieved by reconstructing multiple axial slices and interpolating across the volume.

The authors would like to thank the members of the Center for Light Microscope Imaging and Biology at Carnegie Mellon University. In addition, the authors would like to thank Suresh Santharam for his help in creating the wafer samples. This work was made possible, in part, by the NSF Training Fellowship for Light Microscope Imaging awarded to the first author.

**References**

1. D. Agard, Y. Hiraoka, and J. Sedat. Three-dimensional microscopy: Image processing for high resolution sub-cellular imaging. *Proceedings of SPIE*, 1161:24–30, 1989.
2. V.I. Arnold. *Mathematical Methods of Classical Mechanics*. Springer-Verlag, New York, 2 edition, 1989.
3. Max Born and Emil Wolf. *Principles of Optics*. Pergamon Press, Oxford, 6 edition, 1980.
4. R. Chipman. Mechanics of polarization ray tracing. *Optical Engineering*, 34(6):1636–45, 1995.
5. Carol J. Cogswell, Nicholas Smith, Kieran Larkin, and P. Hariharan. Quantitative dic microscopy using geometrical phase shifter. *Proceedings of SPIE*, 2984:72–81, 1997.
6. C.J. Cogswell and C.J.R. Sheppard. Confocal differential interference contrast microscopy: including a theoretical analysis of conventional and confocal dic imaging. *Journal of Microscopy*, 165(1):81–101, 1992.
7. N. Douglas, A. Jones, and F.van Hoesel. Ray-based simulation of an optical interferometer. *Journal of the Optical Society of America, A*, 12(1):124–131, 1995.
8. A. Erhardt, G. Zinser, D. Komitowski, and J. Bille. Reconstructing 3-d light microscopic images by digital image processing. *Applied Optics*, 24(2):194–200, 1985.
9. Patricia Feinegle. *Motion analysis and visualization of biological structures imaged via Nomarski Differential Interference Contrast Light microscopy*. PhD thesis, Carnegie Mellon University, 1996.
10. J. Foley, A. van Dam, S. Feiner, and J. Hughes. *Computer Graphics*. Addison Wesley, Massachusetts, 2 edition, 1990.
11. William Galbraith. The image of a point of light in differential interference contrast

- microscopy:computer simulation. *Microscopica Acta*, 85(3):233–54, 1982.
12. J.W. Goodman. *Introduction to Fourier Optics*. McGraw Hill, New York, 1996.
  13. Y. Hiraoka, J. Sedat, and D. Agard. Determination of three-dimensional imaging properties of a light microscope system. *Biophysics, J*, 57:325–333, 1990.
  14. Thomas J. Holmes and W. J. Levy. Signal-processing characteristics of differential-interference-contrast microscopy. *Applied Optics*, 26(18):3929–39, 1987.
  15. Shinya Inoue and Kenneth Spring. *Video microscopy: The fundamentals*. Plenum Press, New York, 1997.
  16. Morris Kline and Irvin Kay. *Electromagnetic Theory and Geometrical Optics*. Interscience Publishers, New York, 1965.
  17. Frederick Lanni and H. Ernst Keller. *Microscopy and microscope optical systems*. 1999.
  18. James McNally, C. Preza, J.A. Conchello, and Jr. L. J. Thomas. Artifacts in computational optical-sectioning microscopy. *Journal of the Optical Society of America, A*, 11(3):1056–1067, 1994.
  19. M.L.Dias. Ray tracing interference color. *IEEE Computer Graphics and Applications*, pages 54–60, 1991.
  20. M. Pluta. *Advanced Light Microscopy*, volume 2. Elsevier Science, New York, 1988.
  21. Chrysanthe Preza. *Phase Estimation Using Rotational Diversity for Differential Interference Contrast Microscopy*. PhD thesis, Washington University, 1998.
  22. Rogers and J.A. Adams. *Mathematical Elements for Computer Graphics*. McGraw Hill, New York, 1990.
  23. Maria C. Simon. Ray tracing formulas for monoaxial optical components. *Applied Optics*, 22(2):354–360, 1983.

24. J.D. Trolinger, R. Chipman, and D.K.Wilson. Polarization ray tracing in birefringent media. *Optical Engineering*, 30(4):461–466, 1991.
25. W.Press, S. Teukolsky, W. Vetterling, and B. Flannery. *Numerical Recipes in C*. Cambridge University Press, Cambridge, 2 edition, 1992.